High-Current Density Performance of a Magnetically Shielded Hall Thruster

Leanne L. Su,*[ORCID] Parker J. Roberts,[†] Tate M. Gill,[‡] William J. Hurley,[†] Thomas A. Marks,[§]
Christopher L. Sercel,[§] Madison G. Allen,[†] Collin B. Whittaker,[†][ORCID] Eric Viges,[¶]
and Benjamin A. Jorns[**]
University of Michigan, Ann Arbor, Michigan 48109

The performance of a magnetically shielded Hall thruster operating on xenon and krypton is characterized at discharge current densities up to 10 times greater than its nominal level. A thrust stand and far-field probe suite are employed to evaluate operation at 300 V discharge voltage and discharge currents from 15 to 125 A (xenon) and from 15 to 150 A (krypton). The thrust, specific impulse, and anode efficiency at the highest currents are found to be 1650 ± 30 mN, 2309 ± 56 s, and 52.8 ± 2.0% respectively for xenon, and 1839 ± 18 mN, 2567 ± 48 s, and 55.0 ± 1.6% for krypton. The thrust density at the highest conditions are shown to be six (xenon) and eight (krypton) times higher than the lowest current condition. A maximum in anode efficiency as a function of discharge current is observed for both gases. This is attributed to a trade between mass utilization, which increases to unity with current, and beam utilization, which gradually decreases with current. The dependence of these efficiency modes on current is discussed in the context of a series of first-principles scaling laws. The observation that efficiency only moderately decreases with current density is examined in the context of high-power electric propulsion development.

Nomenclature

A	=	discharge channel area
B	=	magnetic field
E	=	electric field
e	=	elementary charge
g_0	=	gravitational acceleration
I_b	=	ion beam current
I_c	=	characteristic current
I_d	=	discharge current
I_e	=	electron current
I_n	=	current contribution from nth species
I_{sp}	=	specific impulse
$\bar{I}_d$	=	adjusted discharge current
j_i	=	ion-current density
k_B	=	Boltzmann constant
k_{en}	=	electron-neutral rate coefficient
k_{iz}	=	ionization rate coefficient
L	=	discharge channel length
m_e	=	electron mass
m_i	=	ion mass
$\dot{m}$	=	total neutral mass-flow rate
$\dot{m}_a$	=	anode neutral mass-flow rate
$\dot{m}_b$	=	ion beam mass-flow rate
$\dot{m}_c$	=	cathode neutral mass-flow rate
$\dot{m}_{fac}$	=	facility mass-flow rate
n_e	=	electron number density
n_i	=	ion number density
n_n	=	neutral number density
P	=	total power
P_{cool}	=	cooling power
P_d	=	discharge power
P_{mag}	=	magnet power
q	=	charge
T	=	thrust
T_e	=	electron temperature
T_g	=	neutral gas temperature
V_a	=	acceleration voltage
V_d	=	discharge voltage
V_p	=	plasma potential
V_{i-g}	=	ion energy relative to ground
v_e	=	electron velocity
v_i	=	ion velocity
v_n	=	neutral velocity
Z_n	=	nth charge state
z	=	axial distance
η_a	=	anode efficiency
η_b	=	beam-current utilization efficiency
η_c	=	cathode flow efficiency
η_d	=	plume divergence efficiency
η_m	=	mass utilization efficiency
η_p	=	magnet power efficiency
η_q	=	charge utilization efficiency
η_v	=	voltage utilization efficiency
$\eta_{a,probe}$	=	anode efficiency as measured by probe suite
$\eta_{a,thrust}$	=	anode efficiency as measured by thrust stand
$\eta_{b,B}$	=	beam-current utilization efficiency with Bohm scaling
$\eta_{b,c}$	=	beam-current utilization efficiency with classical scaling
η_{fac}	=	facility correctional efficiency
η_{tot}	=	total efficiency
θ	=	Azimuthal probe location
θ_d	=	plume divergence angle
ν_e	=	electron collision frequency
$\nu_{e,B}$	=	Bohm scaling-electron collision frequency
$\nu_{en,c}$	=	classical electron-neutral collision frequency
Ω_e	=	Hall parameter
Ω_n	=	nth current fraction
ω_{ce}	=	electron cyclotron frequency

*Ph.D., Department of Aerospace Engineering; leannesu@umich.edu.
†Ph.D. Candidate, Department of Aerospace Engineering. Student Member AIAA.
‡Research Scientist, Department of Aerospace Engineering.
§Postdoctoral Research Fellow, Department of Aerospace Engineering.
¶Senior Research Engineer, College of Engineering.
**Associate Professor, Department of Aerospace Engineering; bjorns@umich.edu. Associate Fellow AIAA.

I.   Introduction

THE development of high-power (>100 kW), lightweight, and high-performance electric propulsion (EP) technologies is critical for enabling the next generation of deep-space crewed missions. As outlined by the National Academy of Engineering in a commissioned study on nuclear-powered missions to Mars, baseline requirements for future EP systems include input power greater than 2 MW, specific impulse greater than 2000 s, efficiency greater than 50%, and system-specific mass less than 5 kg/kW [1]. Whereas a number of technologies have been proposed to meet these requirements [1,2], the Hall thruster is a particularly promising candidate that has been featured in a recent trade study on a proposed nuclear electric propulsion plan for Mars [3]. Indeed, this thruster class has extensive development and flight heritage at power levels below 12.5 kW [4–7], and laboratory models have been demonstrated up to 100 kW [8–13]. The performance of Hall thrusters, at least in the ∼1–10 kW range, has also been shown to meet the specific impulse and efficiency requirements for near-term nuclear architectures for Mars [1,3].

Despite these attractive capabilities, the achievable thrust density of Hall thrusters remains a major potential limitation for high-power applications. Historically, Hall thruster design has largely been governed by established scaling laws [14–16], including the general principle that nominal operation requires a current density of 100–150 mA/cm^2 [16] in the discharge channel. Modern Hall thrusters typically operate at thrust densities of ∼10 N/m^2 [17], in part due to this design guideline. This is approximately an order of magnitude higher than other mature EP technologies like gridded ion thrusters, which makes Hall thrusters an attractive candidate for the power levels currently available on orbit (<10 kW). However, in the 100 kW–1 MW power range envisioned for nuclear architectures, Hall thruster sizes can become prohibitively large. This limitation has led to other types of thruster technologies, most notably the magneto-plasmadynamic thruster (MPD) and the applied-field MPD thruster (AF-MPD), which have inherently higher thrust densities, to be the default propulsion option for planned high-power applications [3].

If Hall thruster thrust densities could be increased while maintaining performance, however, these devices could represent a competitive and even favorable (given their existing flight heritage) alternative to lower maturity concepts like MPDs. To this end, multiple strategies have been employed to date to increase the thrust density in a Hall thruster. The first of these was to operate at higher discharge voltage while still maintaining the "optimal" level of current density. The TSNIIMASH DL-160, a laboratory water-cooled thruster developed in the 1970s [9,10], followed this approach, demonstrating 140 kW at 8 kV discharge voltage on bismuth with a thruster efficiency greater than 70%. With its 160-mm-diameter channel, this yielded a thrust density of over 100 N/m^2, an order of magnitude higher than the typical thrust density of a Hall thruster operating at 300 V [17]. With that said, the high voltages on this system led to a high specific impulse of ∼8000 s, which corresponds to a thrust-to-power ratio likely too low for a crewed Mars architecture. As an alternative solution, multiple discharge channels can be nested concentrically to increase thrust density and reduce specific mass [18,8]. However, even in the ideal limit where the nesting is sufficiently compact so that the entire thruster surface generates thrust, the increase in thrust density compared to a single-channel thruster of the same size is only a factor of 2. To this point, for the approximate dimensions (Ref. [8]) of the 100-kW X3 nested Hall thruster tested in 2019, the thrust density was the same as the nominal ∼10 N/m^2 typical of single-channel thrusters. As this result and the DL-160 work thus show, attempts to increase thrust density to date have resulted in prohibitively high specific impulse or only marginal improvements. These limitations ultimately can be traced to the fact that the proposed solutions were based on raising thrust density while respecting the design guideline for optimal current density.

There is reason to believe, however, that this restriction on current density may not be absolute. One common justification for this guideline is that increasing the current density decreases electron confinement and therefore leads to a degradation in performance. However, this argument is based on the assumption that the electron dynamics in Hall thrusters scale classically [14], whereas in practice, the electron dynamics in $E \times B$ devices are driven by nonclassical effects [19]. To this point, Simmonds et al. recently performed a theoretical study of the thrust density in Hall thrusters that allow for nonclassical transport [17]. These authors ultimately concluded that the theoretical limit on thrust density is on the order of 1000 N/m^2, two orders of magnitude higher than the current typical value of 10 N/m^2. We also recently established that we were able to increase the current density of a laboratory magnetically shielded Hall thruster by a factor of 2.7 from nominal without a loss in performance [20]. In light of these theoretical arguments, previous exploratory studies, and the major advantages of being able to operate Hall thrusters at higher current density, the need is apparent to systematically explore Hall-thruster operation in this high-current-density regime.

In this work, we modify a 9-kW class magnetically shielded Hall thruster to operate at 45 kW with a 10× increase in nominal current density. We present performance data and plasma plume properties for operation on both xenon and krypton and characterize efficiency trends based on these results. Contributions from this study include a demonstration of the ability to maintain high performance at atypically high current densities and a theoretical discussion of efficiency trends seen for both propellants with increasing current. With these objectives in mind, this article is organized in the following way: In Sec. II, we give an overview of the experimental setup, including the test article, facility, operating conditions, and diagnostics. In Sec. III, we describe our methodology for characterizing the thruster's performance. In Sec. IV, we present the key results of our study, including global performance, indications of thruster health, plasma plume properties, and component efficiencies. Finally, in Sec. V, we discuss physical explanations for our findings, their impacts on our understanding of high-current-density Hall thruster operation, and their implications in the broader context of high-power electric propulsion.

II.   Experimental Setup

We describe in this section the experimental setup for this test campaign. We first overview the test article and the modifications made to adapt it for testing at increased power density. We then describe the test facility and the operating conditions for the thruster. We conclude with a discussion of the diagnostics used to evaluate performance.

A.   Test Article

We employed a modified version of the H9 Hall-effect thruster for this study, the "H9 MUSCLE" (Fig. 1). The baseline 9-kW-class H9 thruster [21,22] was built as a common platform for shared research and investigation into new innovations in Hall thruster technology and physics. As described in Refs. [21–23], the baseline H9 has a stainless-steel anode, graphite pole covers protecting the magnetic circuit, and a centrally mounted LaB$_6$ cathode with a graphite keeper designed for operation up to 60 A [24]. The H9 also employs a magnetically shielded field topology, a method that shapes magnetic field contours to establish a potential gradient directed away from the channel walls [25,26]. This serves to reduce ion-induced erosion on the thruster's channel walls, which has been shown to improve the lifetime of Hall thrusters by an order of magnitude compared to unshielded thrusters [26]. The nominal operating envelope of the H9 operating on xenon includes discharge powers of 4.5–12 kW, specific impulses of 1800–3000 s, thrusts of 290–700 mN, and overall efficiencies of 55–70%. The typical operating envelope with krypton as propellant includes discharge powers of 4.5–9 kW, specific impulses of 1900–2700 s, thrusts of 260–350 mN, and total efficiencies of 45–55% [20–23,27].

We made two modifications to the H9 to facilitate the investigation into high-current- density operation, primarily motivated by the need to accommodate increased thermal loading. First, we replaced the baseline boron-nitride discharge chamber with a graphite discharge chamber. This modification was previously demonstrated with the H9C, a graphite-walled version of the H9 [23]. Second, we implemented an active water-cooling loop inserted adjacent to the magnetic coils in the thruster to maintain low temperatures for the material of the magnetic circuit. This water-cooling loop was connected to the city water flow
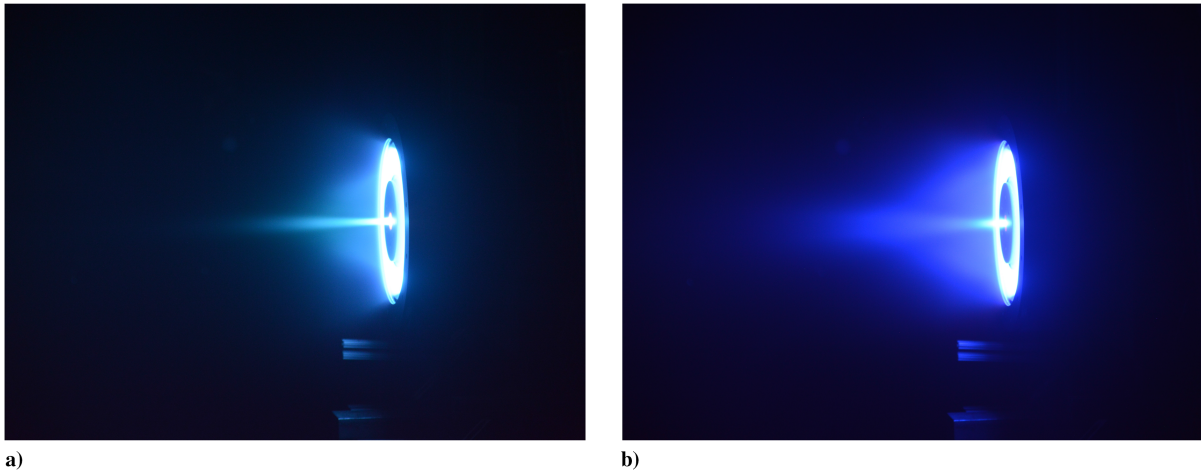
Fig. 1   H9 MUSCLE operating on a) xenon at 300 V and 125 A, and b) krypton at 300 V and 150 A.

and a booster pump that used ∼560 W of power to flow 2.5 GPM. This cooling system was run in open loop at maximum flow rate and no attempts were made to actively control temperature. This approach alleviated excessive thermal loading of the magnetic circuit, which stems from enhanced plasma flux to the channel walls at high current densities, for a sufficiently long duration to perform detailed measurements of thruster operation. The use of water cooling allowed us to focus on the more fundamental question of the role of current density in thruster performance. A similar modification with water cooling was applied in previous laboratory experiments of high-power Hall thruster operation [9,10].
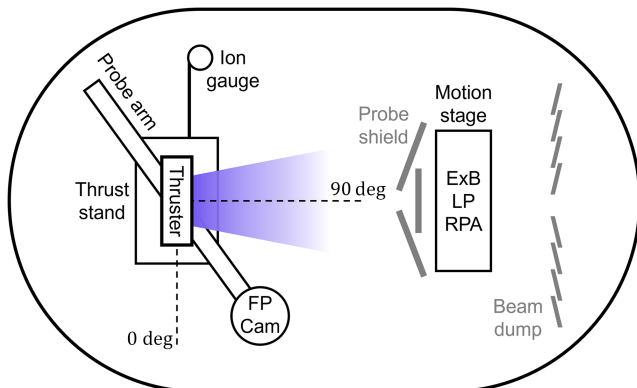

Fig. 2   Notional top-down schematic of experimental setup in the vacuum facility.

B.   Facility

Figure 2 shows a top-down schematic of the experimental setup. We conducted the test in a 6-m-diameter-by-9-m-long steel vacuum chamber with a nominal pumping capacity of 500 kL/s for xenon and 600 kL/s for krypton [28]. The thruster was mounted in the chamber on a thrust stand with its exhaust oriented along the chamber centerline. The plume was directed toward a probe suite located ∼14 thruster channel lengths downstream with an $E \times B$ diagnostic, retarding potential analyzer (RPA), and Langmuir probe (LP). This suite was protected from the beam by a shield of graphite panels, as seen in Fig. 3. We mounted a Faraday probe (FP) on a rotating arm and aligned it vertically to the thruster centerline with its pivot coincident with the thruster exit plane. This arm was capable of sweeping azimuthally at a constant radius 10.5 thruster channel lengths downstream of the thruster, yielding a measurement of the ion-current density as a function of azimuthal position from the FP. A chevroned graphite beam dump held at facility potential was mounted behind the downstream probe suite.

A Stabil ion gauge with a stainless-steel neutralizer tube calibrated for xenon was mounted 1 m from the thruster in the exit plane facing downstream [29]. We note here that it has been found that this orientation may, in contrast to a radially directed probe, result in background-pressure measurements ∼20% higher than the actual values [30]. This would indicate that our estimates of neutral ingestion from the ambient environment may be conservative (see Sec. III). These gauges also have an associated uncertainty of 20% [31]. When operating the thruster on krypton, we applied a correction of 1.48 to gauge readings per the manufacturer guidelines. Pressures measured during this effort ranged from 5 to 32 μTorr (see Table 1). For
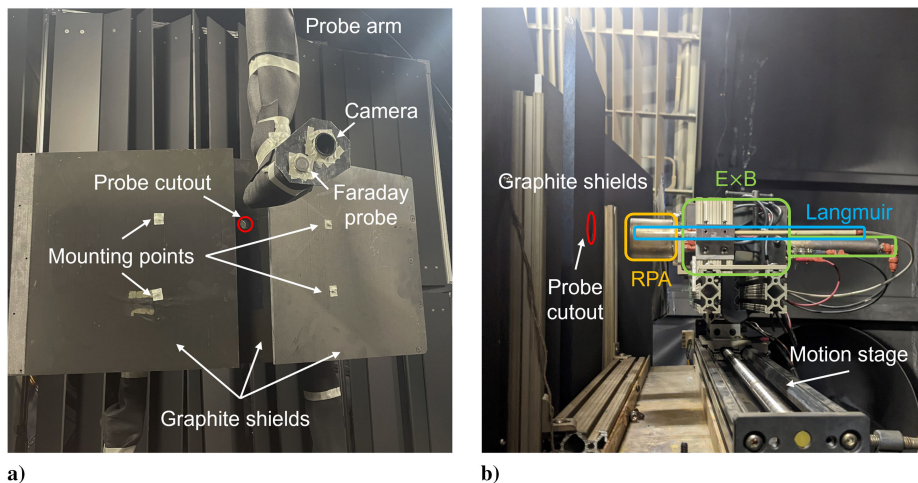

Fig. 3   Probe setup inside the vacuum facility showing a) front view, and b) side view. The side view shows three probes mounted on the motion stage.

Table 1   Operating conditions for test points characterized. The discharge voltage was 300 V for all conditions

Current, A	Power, kW	Xe $\dot{m}_a$, sccm, mg/s	Xe pressure, μTorr-Xe	Kr $\dot{m}_a$, sccm, mg/s	Kr pressure, μTorr-Kr
15	4.5	169, 15.2	5.7	199, 11.4	5.9
50	15	400, 35.9	12.3	537, 30.7	14.5
75	22.5	519, 46.7	16.4	726, 41.5	19.2
100	30	644, 57.9	20.3	885, 50.6	23.7
125	37.5	757, 68.1	23.6	1040, 59.5	28.3
150	45	— —	— —	1193, 68.3	31.8

comparison, these values were slightly higher than pressures previously reported for similar operating conditions on the H9 in this facility [20,27], possibly due to changes in thruster configuration. We employed independently calibrated 3000 and 400 SCCM mass flow controllers for the anode and cathode respectively, each with a reported uncertainty ±0.1% of full scale or ±0.6% of the reading (taking the higher value). Thruster power was supplied by a 150-kW power supply rated to 1000 V and 150 A. The supply was protected from thruster-induced current oscillations by a filter circuit with a 0.3 mH inductor, 47 μF capacitor, and 10 Ω resistor. A series of DC supplies energized the magnets and cathode keeper/heater.

C.   Operating Conditions and Configuration

Table 1 shows the operating conditions we experimentally characterized in this campaign. We operated the thruster at a constant discharge voltage of 300 V for all points and varied the anode flow rate to achieve the target discharge current. The cathode flow fraction was held at 7% for all operating conditions, and we employed a magnetic field strength at 112.5% of its nominal value for this thruster. We operated at this higher magnitude with the goal of attempting to maintain high electron confinement, particularly at higher current densities. We did not attempt to optimize the magnetic field at each operating condition.

The thruster body was electrically tied to facility ground, a necessary configuration resulting from the cooling system we employed. As a general approach, we progressively increased thruster power during the test campaign by increasing the flow and thus discharge current. At each new operating condition, we waited until the mean discharge current achieved a constant value before performing a far-field probe sweep. We then shut down the thruster to take a thrust measurement. Finally, we restarted the thruster and rapidly increased power to the next operating condition. This process typically resulted in a 5-to-15-min dwell time at each operating discharge current higher than 15 A. Although we attempted to achieve the same maximum discharge current conditions for both gases, we were unable to reach the 150-A condition for xenon due to a later-resolved issue in the electrical harnessing. Throughout testing, we monitored peak-to-peak strength of the discharge current oscillations and temperatures of key locations in the thruster body.

We note here that previous work has shown changes in plume properties to be nonlinear with distance from the thruster at high pressures (>10 μTorr) [32,33]. It is immediately evident from Table 1 that even at 50 A (15 kW) of testing power, the pressures in our facility exceed this limit. This underscores the challenges with translating ground test results of high-power systems to be representative of flight. We return to this point in our discussion of FP analysis in Sec. II.D.

D.   Diagnostics

We employed two sets of diagnostics to characterize thruster operation: a thrust stand to measure global performance properties and far-field probes to assess the downstream plume properties. The thrust stand was based on an inverted pendulum design (c.f. Refs. [34–36]) operating in null displacement mode. This stand was calibrated with weights corresponding to an expected thrust range of 10–4800 mN. The major sources for uncertainty in the thrust stand stemmed from variations in the null coil current, uncertainty in the fit to the weights, variance in the displacement drift, and variance in the inclination drift following the methodology outlined in Ref. [37]. From these sources of

uncertainty, we determined that the error in thrust ranged from 14 to 30 mN across all operating conditions.

In the far-field probe suite, the LP consisted of a 1-mm diameter by 4-mm length of tungsten wire extending past an alumina tube. We used this diagnostic to infer plasma potential in the far field V_p from its IV trace following the "Maxwellian" and "knee" methods outlined in Ref. [38], the former of which requires measurements of electron temperature T_e. Due to noise in the raw Langmuir probe data at low currents, we were unable to obtain a clean estimate of plasma potential with the knee method at every condition, and so report only the plasma potential as calculated by the Maxwellian method. We took the variance in the two methods from conditions where we were able to obtain knee values of the plasma potential as the uncertainty for the values reported in this work.

We employed a four-grid RPA (additional details provided in Ref. [36]) with an aperture diameter of 6.45 cm^2 to determine the ion energy distribution function (IEDF) on the thruster channel. From this distribution, we inferred the average ion energy per charge with respect to ground V_{i-g} by averaging the part of the IEDF where the amplitude was over half of the maximum value [39]. By subtracting the local plasma potential V_p (inferred from the LP), we related this measurement to the average kinetic energy of ions in the thruster beam by way of the acceleration voltage, $V_a = V_{i-g} - V_p$. To determine uncertainty in these estimates for ion kinetic energy, we employed a bootstrapping method [40] with a thousand iterations on the inferred IEDF. The reported uncertainties represent the 95% credible intervals, corresponding to twice the standard deviation.

The $E \times B$ probe we employed for this study had an entrance aperture of 1.6 mm in diameter. This diagnostic served as an effective mass charge spectrometer, allowing us to determine the ratios of different charge species within the thruster plume. To extract this data from $E \times B$ telemetry, we followed the approach of Refs. [39,41], in which we fit dual Gaussian distributions to each peak in the processed current trace. One distinction from the methodology we applied in our previous work [27,36] is that we adopt here the integration method detailed in Ref. [41]. We divide the raw current signal by the voltage signal to the third power. In contrast, our previous method of fitting to the raw current trace implicitly assumes narrow velocity distribution functions [41], which are violated at higher current densities. We accounted for the presence of finite background pressure and its impact on charge exchange (CEX), following the methodologies outlined in Refs. [27,41,42], with charge exchange cross-section values taken from Refs. [27,43,44]. The uncertainty in the resultant current fractions primarily stems from fit uncertainty and a 20% uncertainty on the pressure reading within the chamber, typical for the type of gauge used [31].

The azimuthally translating FP consisted of a 2.38-cm-diameter collection disk surrounded by a guard ring. We determined the local ion flux from the thruster with this probe by measuring the current when both collector and guard ring were both biased to -30 V relative to facility ground. We converted this measured current to ion-current density $j_i(\theta)$ per the procedures given in Ref. [45], where θ denotes the angle of the probe arm with respect to the thruster exit plane. Corrections for geometric and secondary electron emission (SEE) effects on the current density were calculated following the methodology outlined in Refs. [27,45] with values of SEE coefficients taken from Refs. [46,47].

We used the angular current density profiles from the FP sweeps to infer two key properties of the thruster: the total ion beam current and

the divergence angle of the plume. For the beam current, we used the formulation

$$I_b = 2\pi R^2 \int_0^{\pi/2} j_i|_{\text{CEX}}(\theta) \cos\theta \, d\theta \tag{1}$$

where R is the distance from the exit plane of the thruster to the probe and $j_i|_{\text{CEX}}(\theta)$ is a corrected current density profile that accounts for the presence of charge exchange collisions in the plume. There are a number of different ways to isolate the contribution of beam ions from CEX ions in the plume, including a flat subtraction [48], an exponential fit [39], and Gaussian fit [45]. In our work, we employed an ensemble modeling approach by averaging the beam current as calculated by all three methods. We estimated uncertainty in the calculated beam current by sweeping the probe across the plume twice, dividing the Faraday sweeps into four 90-degree increments, and determining the average beam current from Eq. (1) from each segment based on the three different CEX correction methods. The reported uncertainty is twice the standard deviation of these four values divided by the number of samples. We note here that we assume symmetry along centerline in the thruster plume.

We estimated the divergence angle of the plume from thruster centerline θ_d following Ref. [45]:

$$\cos\theta_d = \frac{\int_0^{\pi/2} j_i|_{\text{exp}}(\theta) \cos\theta \sin\theta \, d\theta}{\int_0^{\pi/2} j_i|_{\text{exp}}(\theta) \cos\theta \, d\theta} \tag{2}$$

where we have used only the exponential corrected form of the current density from the FP data, $j_i|_{\text{exp}}(\theta)$. In this case, we follow Ref. [39] to correct the current density by fitting an exponential to the trace at large angles. We adopt this approach as it has been shown to yield a higher-fidelity estimate for divergence if there is only data available from an FP sweep performed at one fixed radius. In contrast, the Gaussian and subtraction fit methods, although reliable for beam-current estimates, have not been shown to yield accurate estimations of a divergence angle unless multiple radial sweeps are available [27,45,48]. As with the beam current, we calculated the divergence angle over four 90-deg increment segments. We estimated the uncertainty in the angle as twice the standard deviation in the resulting dataset.

We note here that the best recommended practices for extracting the divergence angle and beam current from FP measurements includes performing sweeps at multiple axial distances downstream of the thruster and extrapolating to the thruster exit [33,45]. In our case, we used only a singular axial FP sweep due to concerns about high operating temperatures and flow rates of the thruster. The lack of axially resolved spatial information likely introduces error in our beam-current and divergence-angle measurements, particularly at the elevated background pressures we encountered at discharge currents above 50 A [33]. Our use of multiple modeling methods is an attempt to allow for variance stemming from these pressure effects, which in turn is reflected by the relatively high uncertainty in the reported measurements.

III. Performance Metrics

We describe in the following section the analytical framework for converting the telemetry from the diagnostics described in the preceding section into assessments of thruster performance and efficiency modes.

A. Global Performance Metrics

The thrust T as determined by the thrust stand measures the total force produced by the thruster. From this measurement, we also can determine the specific impulse (an indication of propellant efficiency) and total efficiency for the thruster (conversion rate of power to directed kinetic energy):

$$I_{\text{sp}} = \frac{T}{\dot{m} g_0} \quad \eta_{\text{tot}} = \frac{T^2}{2\dot{m}P} \eta_{\text{fac}} \tag{3}$$

where $\dot{m} = \dot{m}_a + \dot{m}_c$ is the total mass flow rate from anode and cathode; g_0 is the gravitational acceleration; $P = P_d + P_{\text{mag}} + P_{\text{cool}}$ is the total power to the thruster discharge, magnets, and cooling system; and η_{fac} is a correction factor to account for neutral ingestion from ambient gas in the facility. We estimated this last term following the approach outlined in Refs. [49,50] that was adapted to our test facility [28]. It ultimately contributed less than 0.5%, even at the highest flow-rate conditions.

To assess the operation exclusively for the discharge channel without the effect of losses from the magnet/cooling-system power and cathode flow, we also determine in this work the anode efficiency:

$$\eta_a = \frac{T^2}{2\dot{m}_a P_d} \eta_{\text{fac}} \tag{4}$$

The anode and total efficiencies are related by $\eta_{\text{tot}} = \eta_a \eta_c \eta_p$, where the cathode flow efficiency is $\eta_c = (\dot{m}_a / \dot{m})$ and the power efficiency is $\eta_p = (P_d / P)$. The discharge power is the product of discharge voltage and discharge current, $P_d = V_d I_d$.

B. Efficiency Modes

To provide insight into the physical processes that drive trends in thruster efficiency, we adopt in this work the representation developed [16,51,52] for the dominant efficiency modes in a Hall thruster:

$$\eta_a = \eta_b \eta_q \eta_m \eta_v \eta_d \tag{5}$$

Here, η_b is the beam-current utilization efficiency, η_q is the charge utilization efficiency, η_m is the mass utilization efficiency, η_v is the voltage utilization efficiency, and η_d is the plume divergence efficiency. We review in the following section the physical significance of each of these terms.

1. Beam-Current Utilization Efficiency

This metric represents the ratio of ion current in the thruster channel to the discharge current:

$$\eta_b = \frac{I_b}{I_d} = \frac{I_d - I_e}{I_d} \tag{6}$$

where I_b is the ion beam current in the thruster plume inferred from the FP (Sec. II.D) and I_e is the electron current emitted by the cathode that is in addition to the current required for beam neutralization. This efficiency captures the fact that an electron current that does not contribute to thrust is required to sustain the discharge. Physically, lower values of beam utilization efficiency correspond to reduced electron confinement in the thruster channel. Historically, this efficiency has been believed to be a major driver for degraded performance at higher current density [14–16].

2. Charge Utilization Efficiency

This efficiency mode is due to the presence of multiply charged ion species in the beam:

$$\eta_q = \frac{\left(\sum_n \frac{\Omega_i}{\sqrt{Z_n}}\right)^2}{\sum_n \frac{\Omega_n}{Z_n}} \tag{7}$$

where Z_n is the charge state of the nth ion species and $\Omega_n = (I_n / I_d)$ is the current fraction of the nth ion species inferred from the $E \times B$ probe (Sec. II.D). This efficiency suffers when the ion beam is not monoenergetic.

3. Mass Utilization Efficiency

This parameter is the ratio of beam ion mass flux to neutral mass flux through the anode:

$$\eta_m = \frac{\dot{m}_b}{\dot{m}_a} = \frac{\frac{m_i I_b}{e}\sum_n \frac{\Omega_n}{Z_n}}{\dot{m}_a}\eta_{\mathrm{fac}} = \xi\eta_b\sum_n \frac{\Omega_n}{Z_n}\eta_{\mathrm{fac}} \qquad (8)$$

where $\dot{m}_b$ is the ion beam mass flow rate, m_i is the ion mass, e is the elementary charge, and $\xi = (I_d m_i / e\dot{m}_a)$ is a value defined as the exchange ratio. This efficiency mode is due to the fact that not all neutrals are ionized and accelerated out of the channel. These un-ionized particles do not significantly contribute to thrust. We measured the beam current for this efficiency mode with the Faraday probe and the current fractions with the $E \times B$ probe. We note that like the anode and total efficiencies, the mass utilization is corrected by η_{fac} to account for neutral ingestion.

4. Voltage Utilization Efficiency

This metric is the ratio of average acceleration voltage V_a, a measure of the ion energy, to the total discharge voltage:

$$\eta_v = \frac{V_a}{V_d} \qquad (9)$$

This efficiency mode stems from the fact that not all of the applied discharge voltage from the power supply is available to accelerate ions. This efficiency is decreased by ions born downstream of the peak potential and by the voltage required to extract electrons from the cathode. We determined the average acceleration voltage from the far-field RPA and LP.

5. Plume Divergence Efficiency

This efficiency mode relates to the average divergence angle of the plume θ_d:

$$\eta_d = (\cos\theta_d)^2 \qquad (10)$$

This efficiency physically represents the fact that only axially directed momentum imparts thrust. We measured this divergence with the exponential fit method for the ion-current density profile as inferred from the FP (Sec. II.D).

In summary, the product of these efficiency modes will in principle yield the measured anode efficiency. The ability to isolate these modes provides direct insight into which physical processes dominate the response of thruster performance with changing discharge current. Armed with these definitions, we present our results in the next section.

IV.   Results

We present in this section the results of our experimental characterization of the thruster operating on both xenon and krypton at 300 V and discharge currents ranging from 15 to 150 A. We first report on the global performance metrics of thrust, specific impulse, and efficiency. We then show the current oscillations of the thruster at all operating conditions. Finally, we present the processed results of plasma parameters from individual probe measurements, which we also convert into estimates for the thruster efficiency modes.

A. Global Performance

Figure 4 presents the thrust, specific impulse, anode efficiencies, and total efficiencies for both propellants at all conditions. The tabulated values from these plots are available in the Appendix (Tables A1 and A2). As can be seen from Fig. 4a, the thrust trends approximately linearly across the range of currents for each propellant. The xenon thrust exceeds krypton at all discharge currents; at the maximum current where we tested both gases, 125 A, xenon reaches 1650±30 mN and krypton 1582±16 mN. Krypton achieves the maximum overall thrust recorded from this effort with a value of 1839±18 mN at the 150-A condition. We note here that the thrust for both propellants measured at the 4.5 kW condition are about 10–20 mN (or 4–9%) lower than those previously measured on the H9 [27]. We attribute this discrepancy to differences between the baseline H9 and the modified H9 MUSCLE, such as changes in material and electrical configuration. Most saliently, this may have been caused in part by the change from a boron nitride to graphite chamber, which has been shown to slightly decrease performance on other shielded thrusters [23,53].

As shown in Fig. 4b, the specific impulse values measured during krypton performance are all higher than that of xenon at the same discharge current, although the difference is within uncertainty at the
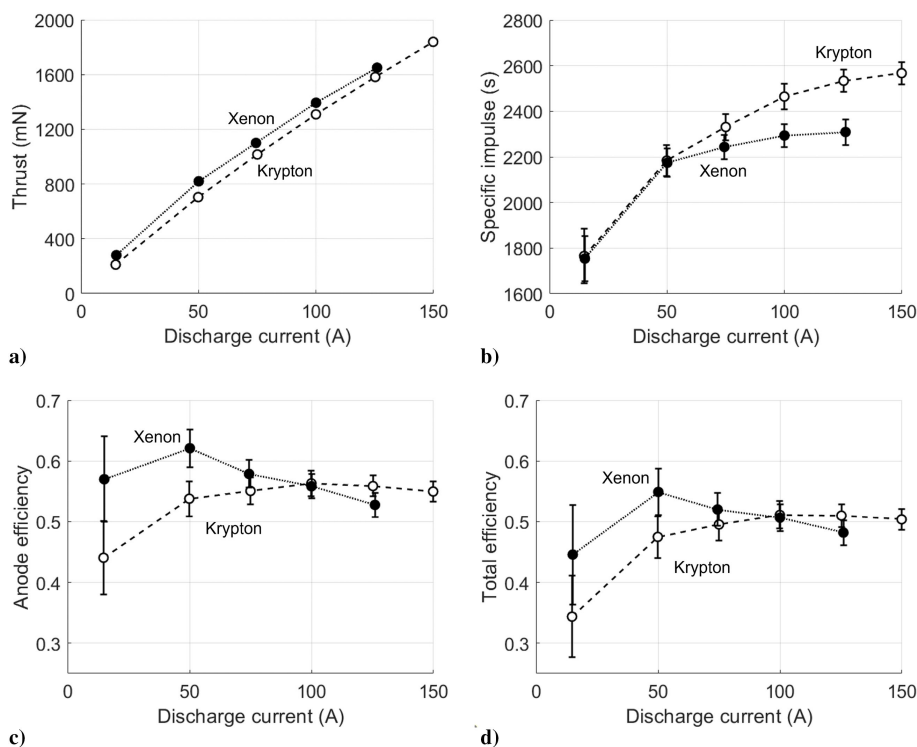

Fig. 4   a) Thrust, b) specific impulse, c) anode efficiency, and d) total efficiency for xenon and krypton at 300 V with increasing discharge current.

15-A and 50-A conditions. At 150 A, krypton operation yields a specific impulse of 2567±48 s. At 125 A, krypton has a specific impulse of 2534±48 s and xenon has 2309±56 s. This disparity can be attributed to the fact that krypton is a lighter atom; becaue the discharge voltage remains the same at each test point, the approximately constant amount of electrostatic acceleration results in higher exit velocities and specific impulse for krypton, the lighter gas. This follows from the relation that the theoretical limit for specific impulse with only singly charged ions is $I_{sp,th} = (\sqrt{2eV_d/m_i}/g_0)$. Similar comparisons between krypton and xenon specific impulse have been reported in previous studies [27,54–56].

With that said, we note that for a beam of only singly charged ions at 300 V, the theoretical limit where all efficiencies are unity is 2000 s for xenon and 2500 s for krypton. However, as shown in Fig. 4b, xenon surpasses this theoretical limit at the 50-A condition, whereas krypton does so at 125 A. We attribute this to the high population of multiply charged species in the beam, particularly for xenon at higher currents (see Sec. IV.C). We discuss this trend in further detail in Sec. V.B.

Figure 4c shows the anode efficiency for both propellants. We remark on four key trends from this data. First, although the efficiency for xenon at its highest discharge current of 125 A is lower than it is at the 15-A condition, the value at the highest current ($\eta_a \sim 53\%$) is still competitive with state-of-the-art designs. The lack of a marked decrease in efficiency with current is direct evidence supporting our hypothesis that the scaling laws historically limiting the increase in current density in Hall thrusters are not absolute. This has direct implications for the achievable thrust density of Hall thrusters at higher powers, a point we expand upon in Sec. V.D. Second, we see that the efficiency of krypton at its highest current condition of 150 A is higher than what is exhibited at 15 A. This trend with increasing current is in line with previous measurements performed on krypton [27,56] and suggests that, for some propellants, performance does not suffer with an order of magnitude higher current density but actually improves. Third, at sufficiently high current, the efficiency of krypton surpasses that of xenon. The efficiency gap between xenon and krypton historically exhibited by Hall thrusters at low currents [27,54–56] thus not only closes at high currents but reverses. Fourth, the efficiency exhibits a maximum with discharge current for both gases. The optimum for xenon occurs at 50 A with an efficiency of 62.1 ± 3.1%, whereas the maximum for krypton is at 100 A with 56.3 ± 2.1%. We conjecture that the non-monotonic trend in efficiency is the result of a trade between improved mass utilization and reduced beam utilization efficiencies. This justification can also explain why krypton, a gas that is more difficult to ionize, exhibits an optimum at higher currents than xenon. We discuss this physical interpretation in further detail in Sec. V.C.

The trends in total efficiency, shown in Fig. 4d, closely mirror the trends in anode efficiency. The maxima are located at the same currents (50 A for xenon and 100 A for krypton) and the crossover point between propellants remains the same at 100 A. The magnitudes are ~4–13% lower than anode efficiency because the total efficiency accounts for the flow through the cathode, and the power supplied to the magnets and the water-cooling booster pump.

B. Thruster Oscillations

In this section, we present measurements of the discharge current oscillation strength, a metric of the thruster's overall stability. We show in Fig. 5 the magnitude of the peak-to-peak oscillations in the discharge current relative to the mean value. The uncertainty of these oscillations was determined by taking twice the standard deviation in the peak-to-peak oscillation strength over 10 s. For xenon, we see that the current oscillations monotonically decreased with discharge current, starting at 69% at 15 A and ending at 4% at 125 A. This latter value is exceptionally low for Hall thrusters [57]. For krypton, the current oscillations generally decreased but exhibited a minor inflection from 75 and 100 A. The oscillation strengths for this gas ranged from 43% at 15 A to 19% at 150 A. From a practical perspective, these measured levels of oscillation show that the thruster did not exhibit unusually high oscillation modes with increasing current density.
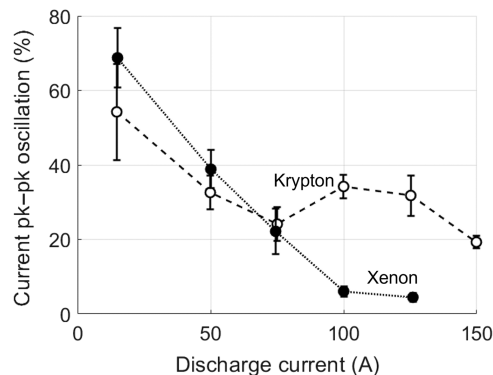

Fig. 5   Ratio of peak-to-peak oscillation to mean value of discharge current for xenon and krypton at 300 V with increasing discharge current.

This suggests that, at least for this configuration, a high-current-density Hall thruster has not only comparatively high performance but is also stable.

As a possible explanation for this behavior, we note that recent work has suggested that for a fixed discharge voltage, thruster stability can improve with higher discharge current; this stems from the fact that the higher local current densities and corresponding high ionization rates help dampen the dominant breathing mode in the thruster [57]. Further, this same work showed that decreasing the residence time of neutrals in the anode can also improve the stability margin. Given the high thermal fluxes heating the anode and the resulting high neutral temperatures, this may also be a contributing factor to the relatively low oscillation levels. This remains a qualitative observation, however, as the high voltages of the anode precluded us from directly evaluating its temperature during this effort.

C. Probe Measurements

We present in this section the measurements of plasma parameters from our far-field probes necessary to evaluate the efficiency modes of the thruster. We first show in Fig. 6 the plasma potential (measured with respect to ground) and electron temperature, as determined from Langmuir probe traces using the methodology outlined in Sec. II.D. Both these plasma properties generally decrease after achieving a maximum value with increasing discharge current.

We show in Fig. 7 the average acceleration voltage inferred from the RPA for both xenon and krypton. In this case, we have made a correction to the RPA measurement with respect to ground by subtracting the local plasma potential as determined by the LP (Fig. 6). The average acceleration voltage V_a is on the order of the applied voltage of 300 V within error bars. Notably, the acceleration voltage generally increases with xenon whereas generally trending down with krypton. This may suggest that the acceleration process for each propellant is impacted in opposing ways by the increasing current density in the thruster.

In Fig. 8, we present the current fractions as determined from the $E \times B$ measurements. For both propellants, we see that the fraction of the singly charged state generally decreases while the populations of multiply charged states increase. Indeed, xenon exhibits a population inversion (i.e., where the fraction of doubly charged ions surpasses that of singly) at 50 A. As we see in Fig. 8b, krypton reaches this point of population inversion at the highest current condition of 150 A. For both propellants, the triply charged population steadily increases with current. We discuss possible physical explanations for these trends with current in Sec. V.A.

Figure 9 shows the plume divergence angles inferred from our FP measurements. For xenon, the divergence monotonically increases with current from 22.5° ± 1.6° at 15 A to 28.2° ± 1.5° at 125 A. In contrast, for krypton, there is a less well-defined trend as discharge current increases. The divergence angle stays nearly constant for all currents, only ranging from a minimum of 26.5° ± 1.2° at 50 A to a maximum of 27.9° ± 1.7° at 150 A. We discuss the implications of these variations in divergence angle in Sec. V.C.
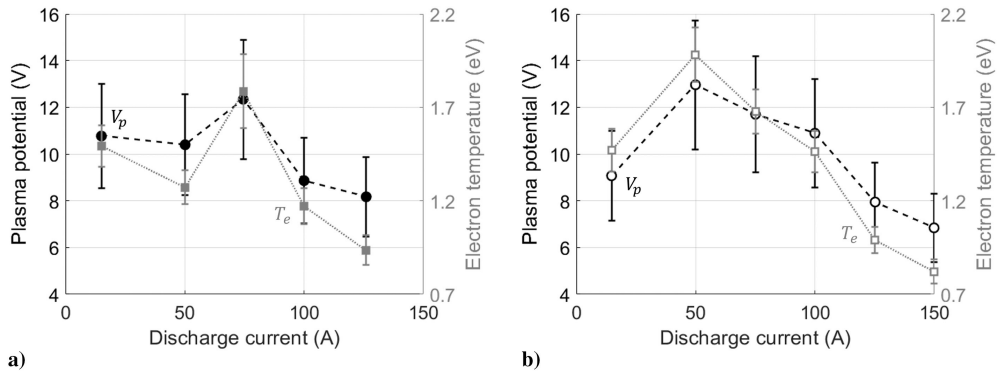
Fig. 6   Plasma potential and electron temperature of a) xenon, and b) krypton at 300 V with increasing discharge current.
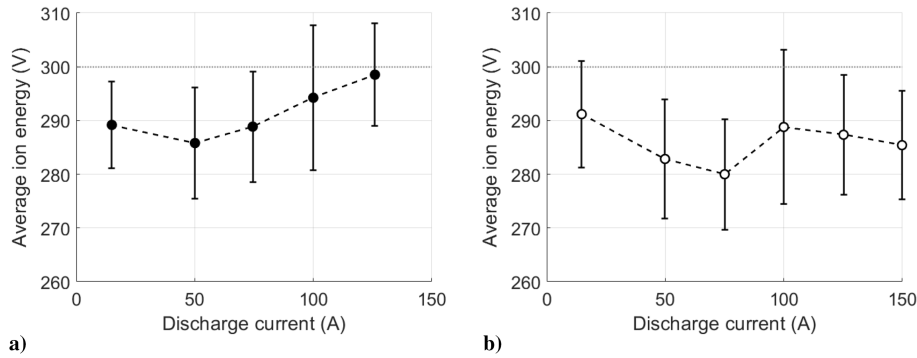

Fig. 7   Average ion energy for a) xenon, and b) krypton at 300 V with increasing discharge current. The discharge voltage is indicated with a dotted gray line.
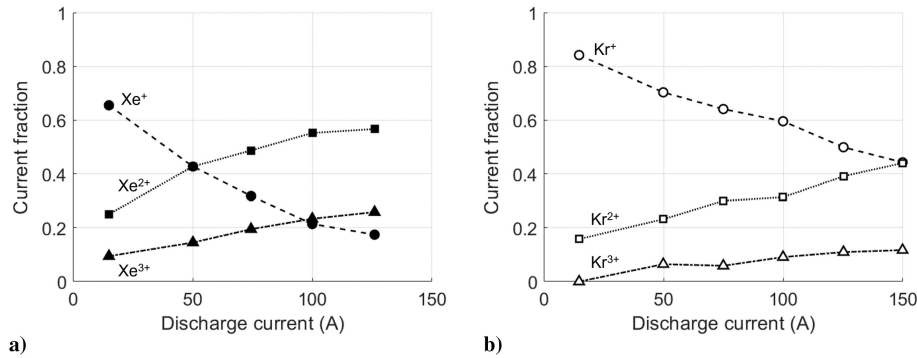

Fig. 8   Current fractions of singly, doubly, and triply ionized a) xenon, and b) krypton at 300 V with increasing discharge current.
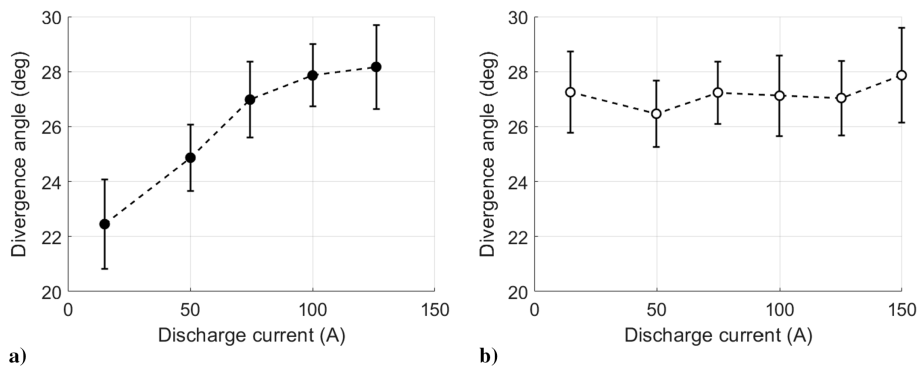

Fig. 9   Plume divergence angle of a) xenon, and b) krypton at 300 V with increasing discharge current.

D.   Efficiency Analysis

Armed with probe measurements from the preceding section, we present here our calculations for the efficiency modes of the thruster. Figure 10 shows these compiled results plotted as a function of discharge current for both propellants. This figure also displays the

anode efficiency as measured directly from thrust, $\eta_{a,\text{thrust}}$ [Eq. (4)], compared to the anode efficiency as calculated by the product of efficiency modes, $\eta_{a,\text{probe}}$ [Eq. (5)]. In all cases, the uncertainties in the plotted values stem from the propagation of experimental error from the probe measurements through the governing equations of the
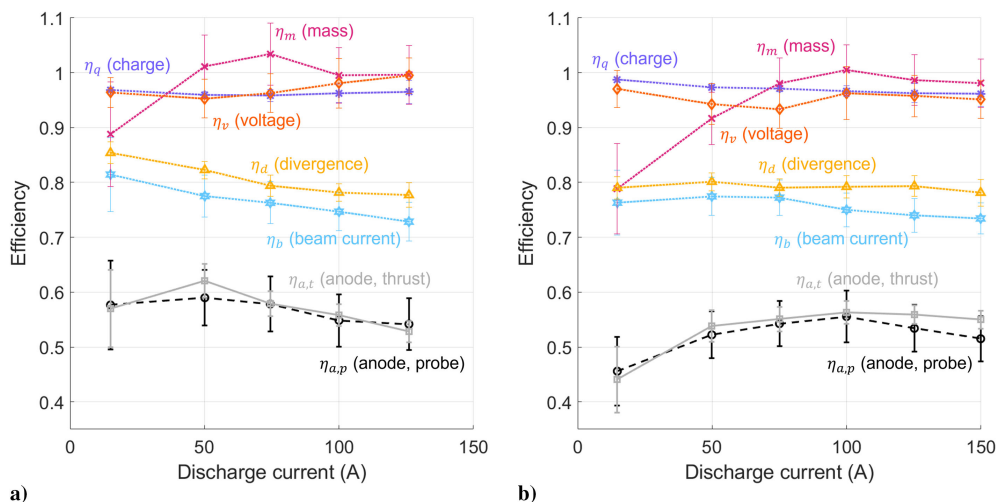
Fig. 10   Efficiency modes for a) xenon, and b) krypton at 300 V with increasing discharge current.

efficiencies (Sec. III.B). The values in these plots, including uncertainty estimates, are tabulated in the Appendix (Tables A3 and A4).

1. Anode Efficiency

The gray lines in Fig. 10 indicate the anode efficiency as determined from direct thrust measurements [Eq. (4)], whereas the black lines indicate the anode efficiency as calculated as the product of efficiency modes [Eq. (5)]. At all conditions, $\eta_{a,\text{probe}}$ and $\eta_{a,\text{thrust}}$ are within uncertainty of each other and generally follow the same trends with increasing current. The minor discrepancies between measurements may in part be due to our assumptions for estimating the key plasma parameters (i.e., charge exchange corrections, only employing a single Faraday probe sweep at fixed radial position, fitting methods for divergence angle, etc.). Regardless, the general agreement indicates that the efficiency model outlined in Sec. III.B is an accurate representation of the performance of the thruster.

2. Beam Current Utilization

Figure 10 shows that the beam current utilization steadily decreases for xenon with increasing current. With krypton, the current utilization efficiency increases from 15 to 50 A before slightly decreasing throughout the higher current conditions. This downward trend in beam utilization efficiency has been observed in previous studies of Hall thruster efficiency at high powers, and the values (∼75%) are in line with what is typically observed on Hall thrusters [16,20,27,33,51,58–61], albeit lower than the previously reported measurements for the H9's baseline condition at 300 V and 15 A [20,27]. The discrepancy at this condition may in part be attributed to differences in the thruster configuration as well as how we performed the beam calculation from the FP traces; in this previous work (Ref. [27]), we adopted a different method for estimating beam current that required multiple radial sweeps of the FP probe.

The trend in beam utilization suggests that electron confinement suffers at higher currents, leading to a higher relative electron contribution to the total current [Eq. (6)]. This behavior is broadly consistent with past phenomenological explanations that have been proposed (c.f. Refs. [14,16]) for the impact of discharge channel plasma density on Hall thruster operation. Indeed, it has been suggested in these works that the higher plasma density associated with higher current density leads to enhanced electron collisionality, and therefore higher degrees of cross-field electron transport. Notably, however, we see that the decrease in the beam utilization efficiency is at most ∼9% over an order of magnitude increase in current. This suggests that the loss of electron confinement is not driving the overall performance to noncompetitive values. Indeed, the relatively gradual downward trend in beam utilization largely explains why the thruster performance has not suffered markedly at these high current conditions, a point further explored in Sec. V.C.

3. Charge Utilization

As can be seen from Fig. 10, the charge utilization is nearly unity for the range of investigated currents. We see that for xenon, there is a minor decrease in charge utilization in the range from 15 to 75 A before increasing again, whereas for krypton, the charge utilization steadily decreases. This behavior can be explained by the relative disparity of charge states; charge utilization ultimately reaches 100% when the beam is monoenergetic, and deviates from this when the beam is polydispersive, i.e., containing differently charged species (see Fig. 8). Ultimately, the change in charge utilization is minimal (<3%) throughout the entire range and therefore not a major contributor to the trends in anode efficiency.

4. Mass Utilization

The mass utilization efficiencies for xenon and krypton are 88.8±9.6% and 78.9±8.2%, respectively, at the 15-A discharge current conditions. For krypton in particular, the mass utilization at this current is its lowest efficiency mode. These values are in keeping with previous measurements on this power class of thruster [27,56]. With increasing current, the mass utilization reaches 100% within uncertainty for both gases. This behavior is physically consistent with the interpretation that the plasma density at these conditions is sufficiently high such that all inlet neutral gas is ionized. Xenon reaches full ionization at 50 A, whereas krypton approaches this level at 100 A. The fact that krypton requires a higher current to reach full ionization is likely due to its smaller cross-section for ionization (see Sec. V.C). However, as the current density and therefore plasma density in the channel increases, the ionization mean free path becomes small enough so that all the neutrals are ionized, even for krypton.

We note here that some of our calculated values for mass utilization slightly exceed 100%, specifically at 50–75 A for xenon and 100 A for krypton. These nonphysical results might be explained by limitations in our approach to deconvolving the impact of CEX ions, the lack of multiple axial distances for our FP sweeps, or discrepancies in the amount of calculated neutral ingestion (see Sec. II.D). Indeed, the flow rates into the facility are exceedingly high compared to most previous Hall thruster testing performed to date, leading to facility pressures well above the recommended 10 μTorr level [32,33]. It thus may not be unexpected that standard convolution methods may be compromised.

Leaving these arguments aside, because all measurements ultimately are within experimental uncertainty of 100%, we work under the assumption in our subsequent discussion that the total mass utilization efficiency is effectively 100% whenever the measured value exceeds this value.

5. Voltage Utilization

As can be seen from Fig. 10, the voltage utilization for xenon generally increases with current. This behavior is consistent with the

trends exhibited in Fig. 7, where we see the average ion energy mostly increase with discharge current. For krypton, all points are within uncertainty of each other (a minimum of $93.3 \pm 3.5\%$ and a maximum of $97.1 \pm 3.4\%$), indicating no evident trend in this efficiency mode with increasing current.

6. Plume Divergence

Figure 10 shows that trends in plume divergence efficiency mirror the trends in divergence angle. This efficiency mode decreases monotonically for xenon with discharge current, whereas it remains approximately constant with current for krypton. In terms of magnitude, this mode is the second-largest detractor to the overall efficiency next to beam utilization. We discuss the possible physical causes for this low divergence efficiency in Sec. V.C.3.

7. Summary of Efficiency Trends

In this section, we have presented the efficiency modes for operation on both xenon and krypton and discussed how they trend with increasing current. At higher-than-nominal currents (>15 A), the lowest efficiency mode for all conditions is the beam utilization efficiency, which generally decreases with increasing current and ranges between 73% and 78%, (excluding the 15-A condition for both propellants). The next-lowest efficiency mode at high currents is the divergence efficiency, which varies from 78% to 82% in the 50–150-A range. The charge and voltage utilization were both above 90% at all conditions for both propellants. Finally, the mass utilization efficiency varied the most with current, generally with a dramatic increase from low to high currents. In Sec. V.C, we focus on the physical drivers behind the mass and beam utilization efficiencies and discuss how they shape the overall trends in thruster performance with increasing current.

V. Discussion

We discuss in this section the key implications of our results. We first provide a physical explanation for the increasing populations of multiply charged species and how this relates to the monotonically increasing specific impulse. Next, we explore the physical drivers behind trends in efficiency, particularly for the mass and beam utilization and briefly for divergence. We conclude with a discussion regarding how our results impact our fundamental understanding of the limits of Hall thrusters operating at high powers and their comparative advantages to other technologies.

A. Trends in Current Fractions

As seen from Fig. 8, the fraction of multiply charged ions increases at higher currents for both propellants. This trend likely results from increasing current densities in the channel, which in turn translates to mass utilization efficiencies approaching unity (see Sec. IV.D.4). With a mass utilization of one, all the inlet propellant is effectively ionized. As the current and therefore plasma density in the channel continue to increase, the resulting singly charged ions can have additional ionization events, thereby gaining additional charge. This could explain the higher densities of multiply charged species.

B. Trends in Specific Impulse

As shown in Fig. 4b, one of the notable findings from of our study is the 30–45% increase in specific impulse with current exhibited by each propellant. To explain this trend, we consider a theoretically informed expression for the specific impulse:

$$I_{\mathrm{sp,th}} = \frac{1}{g_0} \eta_c \eta_m \sqrt{\eta_d \eta_v} \frac{\sum_n \frac{\Omega_n}{\sqrt{Z_n}}}{\sum_n \frac{\Omega_n}{Z_n}} \sqrt{\frac{2eV_d}{m_i}} \tag{11}$$

where we have assumed that thrust contributions from charge species n is given by $T_n = \dot{m}_b \sqrt{(2eZ_n V_a / m_i)} \cos\theta_d$. As this result shows, the specific impulse depends on the cathode flow fraction, mass utilization efficiency, divergence efficiency, voltage utilization efficiency, and relative current fractions for a given propellant and voltage.

In Fig. 11, we show Eq. (11) plotted as a function of current where we have employed the measured efficiencies and current fractions from Sec. IV.D (Figs. 8 and 10). We consider the cases of a singly charged beam (dotted black line), a multiply charged beam (dashed black line), and the limiting cases where the beam is entirely singly and doubly charged with 100% efficiency (horizontal gray lines). The multiply charged beam was determined using the current fractions as inferred from the $E \times B$ probe (Fig. 8).

As this result shows, the trend of increasing specific impulse with discharge current is largely explained, by the increase in mass utilization. This is made evident by considering the linear dependence of specific impulse on mass utilization efficiency seen in Eq. (11) (compared to the weaker dependencies on voltage and divergence efficiency) and how dramatically the mass utilization increases with discharge current (Fig. 10). The increase in mass utilization is caused by enhanced ionization at higher currents leading to more of the inlet gas being converted to plasma, which in turn can be accelerated to generate more thrust. We note, however, that the magnitude of the specific impulse cannot be explained purely by the acceleration of singly charged ions. In fact, the maximum theoretical specific impulse for singly charged species at 300 V is exceeded at the higher current cases for both gases. This result suggests that the polydispersive nature of the plasma is responsible for the higher specific impulse values. Indeed, accounting for the large presence of multiple charge states brings the magnitude of the theoretical value [Eq. (11)] in line with measurement.

A notable implication of this result is that in these high-current-density operating regimes where the plasma is dominated by higher charge states, the effective specific impulse can receive a boost that brings it to values greater than the typical level exhibited by lower-current-density thrusters [42,62,63] without needing to increase the discharge voltage. This has potential benefits for deep space missions, in particular where high specific impulse operation is desirable [1,16].

C. Trends in Efficiency

We present here physical explanations for the observed variations in mass utilization, beam utilization, and divergence efficiency. We frame this discussion in the context of a set of simplified, zero-
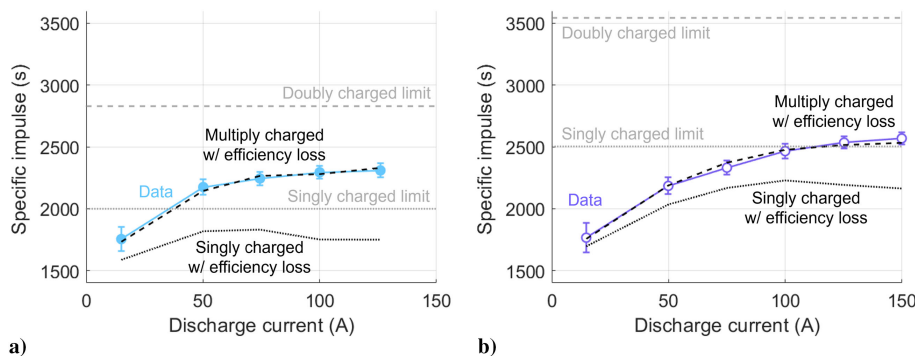

Fig. 11 Experimentally measured values of specific impulse for a) xenon, and b) krypton operating at 300 V compared to theoretical values.

dimensional (0-D) scaling laws for thruster operation as it depends on current.

1. Trends in Mass Utilization Efficiency

We motivate in this section a 0-D model for the mass utilization as it relates to discharge current. To this end, we begin with the quasi-one-dimensional continuity equation (averaged over channel area) for neutral density in the channel at steady state:

$$v_n \frac{\partial n_n}{\partial z} = -k_{iz} n_e n_n \qquad (12)$$

where v_n is the neutral velocity, n_n is the neutral density, z is the axial direction, k_{iz} is the rate coefficient for ionization averaged over a Maxwellian electron velocity distribution, and n_e is the electron density. We next make the strong assumption that the plasma properties are approximately constant axially in the channel so that we can formulate an analytical expression for the neutral density. Integrating Eq. (12) over the length of the channel L thus yields

$$n_n(L) = n_n(0) \exp\left[-\frac{\langle k_{iz} \rangle \langle n_e \rangle}{v_n(0)} L\right] \qquad (13)$$

where $\langle x \rangle$ denotes a volumetrically averaged quantity in the channel, $n_n(0)$ is the inlet neutral density at the anode, and $v_n(0)$ is the neutral velocity at the anode. Physically, this result indicates that the neutral density decays exponentially in the channel with a characteristic length on the order of the mean free path for ionization. Previous numerical work has indeed shown that the axial neutral density profiles are approximately exponential in nature [64,65].

Armed with this expression for neutral density, we can write the mass utilization efficiency in terms of the neutral flow at the end and at the beginning of the channel as

$$\eta_m = 1 - \frac{\dot{m}(L)}{\dot{m}(0)} \approx 1 - \frac{n_n(L)}{n_n(0)} = 1 - \exp\left[-\frac{\langle k_{iz} \rangle \langle n_e \rangle}{v_n(0)} L\right] \qquad (14)$$

where we have used the definition $\dot{m} = v_n n_n A$ where A is the channel area. We also approximate both the neutral velocity and area as constant through the channel, although practically, both values slightly increase through the channel; for velocity, this is due to expansion from the anode to the channel (which has a larger area), and for area, this is due to the chamfer at the exit plane of the thruster that is associated with a larger channel area. Intuitively, however, this result shows that as the dwell time of neutrals in the channel L/v_n or the probability of ionization (dictated by $\langle k_{iz} \rangle \langle n_e \rangle$) increases, the mass utilization will improve.

We convert our expression for η_m to be in terms of discharge current and parameters that are gas-dependent (i.e., m_i and k_{iz}). In rewriting the mass utilization, we first find it useful to obtain an expression for the electron density. We first define the ion velocity for a singly charged beam as

$$\langle v_i \rangle = \sqrt{\frac{qV_a}{m_i}} = \sqrt{\frac{eV_a}{m_i}} \qquad (15)$$

where we have assumed the velocity to be a factor of $\sqrt{1/2}$ lower than the full velocity of a given ion due to averaging over the entire channel. We now invoke quasi-neutrality and the ion velocity to obtain

$$\langle n_e \rangle = \langle n_i \rangle = \frac{I_b}{q \langle v_i \rangle A} = \frac{\eta_b I_d}{A} \sqrt{\frac{m_i}{e^3 V_a}} \sum_i \frac{\Omega_n}{\sqrt{Z_n^3}} \qquad (16)$$

where we have included the superposition of differently charged beams. We have also made the strong assumption that the beam current ($I_b = \eta_b I_d$), which is measured downstream, is constant through the channel. We next define the neutral velocity using the

mean value in one dimension, assuming sonic injection conditions at the anode, giving us

$$v_n(0) = \sqrt{\frac{2k_B T_g}{\pi m_i}} \qquad (17)$$

where k_B is the Boltzmann constant and T_g is the gas temperature at the anode. Leveraging these expressions for density and neutral velocity, we can simplify Eq. (14) to

$$\eta_m = 1 - \exp\left[-\frac{\bar{I}_d}{I_c}\right] \qquad (18)$$

where we have introduced the variables

$$\bar{I}_d = \frac{m_i}{m_{i(Xe)}} \frac{\langle k_{iz} \rangle}{\langle k_{iz(Xe)} \rangle} I_d$$

$$I_c = \frac{1}{m_{i(Xe)} \langle k_{iz(Xe)} \rangle} \frac{A}{\eta_b L} \sqrt{\frac{2e^3 V_a k_B T_g}{\pi}} \frac{1}{\sum_n \frac{\Omega_n}{\sqrt{Z_n^3}}} \qquad (19)$$

Here, $\bar{I}_d$ is an adjusted current that depends on the mass and ionization rate coefficient for each species. This parameter, according to this simplified theory, should be universal in dictating the mass utilization for different propellants. The parameter I_c is a "characteristic current," where T_g is the temperature of the neutral gas at the inlet, $m_{i(Xe)}$ is the xenon mass, and $\langle k_{iz(Xe)} \rangle$ is a constant given by the ionization rate coefficient for xenon at a reference temperature of $T_e = 30$ eV. This characteristic current depends on channel geometry, charge composition, discharge voltage, and temperature of the neutral gas. Some of these parameters vary with discharge current. However, our experimental results have shown that the relative change in discharge current over the current range is 10 times greater than the variations in beam utilization efficiency, summation over charge states, and the acceleration voltage. We therefore approximate in Eq. (18) the characteristic current I_c as weakly varying and thus approximately constant with current.

We plot the experimental measurements of mass utilization as a function of the adjusted current $\bar{I}_d$ in Fig. 12. To evaluate this current for each gas, we have made the assumption that the electron temperature in eV scales with the discharge voltage by a factor of 0.1 (Refs. [16,66–69]) so that $T_e = 30$ eV for both gases. For comparison, we also plot Eq. (18), where we have empirically calibrated $I_c = 6$ A to achieve a best fit of the data over all measured conditions shown in Table 1. This result illustrates that the xenon and krypton data collapse onto the same curve when we use $\bar{I}_d$, and the agreement between the shape of the theoretical curve and the data lends support to this simplified but physics-motivated description of mass utilization efficiency.
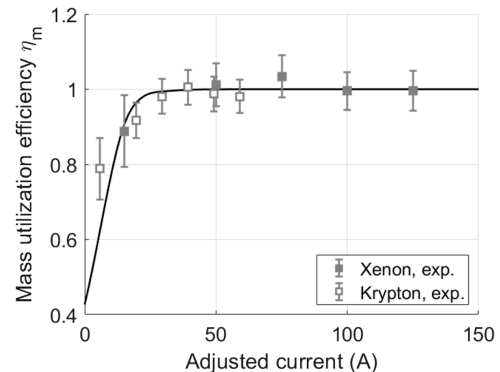

Fig. 12 Experimentally measured mass utilization efficiency for a) xenon, and b) krypton operating at 300 V compared to theoretical forms calibrated on data from Table 2.

Table 2   Plasma parameter values averaged over all operating conditions and both propellants

Parameter	Value
T_g	400 K
$\eta_{b,\mathrm{const}}$	0.75
Ω_1	0.5
Ω_2	0.4
Ω_3	0.1
V_a	290 V
$\langle T_e \rangle$	30 eV
$\langle k_{iz(Xe)} \rangle$	1.079×10^{-13} m³/s
$\langle k_{iz(Kr)} \rangle$	6.651×10^{-14} m³/s

As an additional validation, we use our experimental measurements of the terms in Eq. (19) to calculate a theoretical value of I_c and evaluate if the fit value for our characteristic current is plausible. We obtained these measured values, shown in Table 2, by averaging the data shown in Figs. 6, 8, and 10 over all discharge currents for both propellants. We also assume 400 K for the temperature of the anode as we have in previous work [70,71], although we note that the actual temperatures may be higher due to the atypically high current densities we were operating at. With these averaged values, we find a value of $I_c = 2.2$ A. This is within a factor of 3 of the best-fit value. The discrepancy between the calculated and best-fit parameters can likely be attributed to the several simplifications and assumptions made in our analysis. For example, the $T_e \approx 0.1 V_d$ relation is typically used to approximate the peak electron temperature in the channel. Because we are averaging across the channel, we may therefore expect the effective electron temperature (and therefore ionization rate coefficient) to be lower than 30 eV. This would increase our calculated value of characteristic current I_c to be more in line with our best-fit value of 6 A. We also assumed a form for the average ion velocity in the channel [Eq. (15)] and for the neutral velocity at the inlet [Eq. (17)].

There are two key physical insights that emerge from our 0-D validated description for the mass utilization. The first is that the increase in mass utilization with current can be attributed to the fact that the number density of particles in the channel also increases with current. This higher density of particles facilitates more ionization of the inlet neutral gas. With sufficiently high discharge current for a given gas, all particles are ionized, and the mass utilization approaches unity. This is reflected by the exponential dependence of Eq. (18) on current.

The second insight is that the current required to achieve a fixed level of mass utilization is species dependent. For example, we saw experimentally that the mass utilization of xenon reaches 95% at $\sim$30 A (Fig. 10). For krypton, this occurs at $\sim$70 A, yielding a ratio of $(I_{d(Kr)}/I_{d(Xe)}) \approx 0.43$. This is consistent with the theoretical calculation for current ratio at 300 V:

$$\frac{I_{d(Kr)}}{I_{d(Xe)}} = \frac{m_{i(Kr)}}{m_{i(Xe)}} \frac{\langle k_{iz(Kr)} \rangle}{\langle k_{iz(Xe)} \rangle} \approx 0.39 \tag{20}$$

The need for higher current to achieve full ionization with krypton is firstly because it is more difficult to ionize with its smaller cross-section, and secondly because of its shorter residence time in the channel due to its smaller mass. As an extension from this result, we see that the increase in current density appears to be able to compensate for the traditional mass utilization losses associated with gases with lower ionization cross-sections. This physical phenomenon has been suggested in previous work [72].

2. Trends in Beam Utilization Efficiency

As noted in the preceding Sec. IV.D.2, the beam utilization decreases with increasing current, a likely indication of reduced electron confinement in the channel. We discuss in this section possible physical explanations for this trend. To this end, we begin by writing the definition of beam utilization as

$$\eta_b = \frac{1}{1 + \frac{I_e}{I_b}} \tag{21}$$

We can rewrite this result by adapting Eq. (16) to find an expression for I_b and by using a generalized Ohm's law averaged over the channel to find an expression for I_e. We first solve for the electron velocity v_e by beginning with Ohm's law:

$$0 = -en_e(\boldsymbol{E} + \boldsymbol{v}_e \times \boldsymbol{B}) - m_e n_e \nu_e v_e \tag{22}$$

assuming steady state and no electron pressure gradient but including a collision term. By solving Ohm's law in the azimuthal and axial directions individually, we find the electron velocity in the axial direction to be

$$v_{ez} = -\frac{\frac{e}{m_e \nu_e}}{\Omega_e^2 + 1} E \tag{23}$$

Noting that typically the Hall parameter $\Omega_e = \omega_{ce}/\nu_e \gg 1$ in Hall thrusters, this simplifies to

$$v_{ez} = \frac{1}{\Omega_e} \frac{E}{\langle B \rangle} \tag{24}$$

By invoking $I_e = e n_e v_e A$ and taking an average over the channel, we find

$$I_e = e \langle n_e \rangle \frac{\langle \nu_e \rangle}{\langle \omega_{ce} \rangle} \frac{V_a}{L \langle B \rangle} A \tag{25}$$

where we have approximated the electric field in the axial direction in the channel as $E \approx V_a/L$. We note here that this is a calculation of the total electron current in the channel and therefore a conservative estimate of I_e, but can still provide insight on trends with various plasma parameters. Together, these expressions for beam current and electron current yield

$$\eta_b = \frac{1}{1 + a \sqrt{m_i} \langle \nu_e \rangle} \tag{26}$$

where we have defined the parameter

$$a = \sqrt{\frac{V_a}{e^3}} \frac{m_e}{\langle B \rangle^2 L} \sum_n \frac{\Omega_n}{\sqrt{Z_n^3}} \tag{27}$$

Here, ν_e is the electron collision frequency, ω_{ce} is the electron cyclotron frequency, B is the magnetic field strength, and $\langle x \rangle$ again denotes a plasma property averaged over the channel length. As with our discussion in the preceding section, we again assume V_a and Ω_n to be weakly varying with current such that the parameter $a = 5.8 \times 10^4 \sqrt{(\mathrm{m/N})}$ is approximately constant for our operating conditions (see Table 2).

Physically, Eq. (26) represents the intuitive result that a higher rate of electron collisions ν_e reduces beam utilization, whereas a stronger magnetic field B improves it. Because the magnetic field for our operating conditions was fixed, the key question for relating beam utilization to discharge current is how the average electron collision frequency $\langle \nu_e \rangle$ depends on this current. With that said, the nature of this effective electron collision frequency is poorly understood and still an active area of research [19]. In the absence of a first principles model for this transport coefficient, we consider in this discussion two possible scalings that represent limiting cases for the electron dynamics:

$$\nu_{e,c} = c_c \sqrt{m_i} k_{\mathrm{en}} \frac{\eta_b}{\eta_m} I_d \qquad \nu_{e,B} = c_B \tag{28}$$

where k_{en} is the electron-neutral rate coefficient, which is dependent on species and electron temperature, and we have defined parameters that are approximately constant with current,

$$c_c = \alpha_c \frac{\sqrt{\pi} \sum_n \frac{\Omega_n}{Z_n}}{\sqrt{2 k_B T_e} eA} \quad c_B = \alpha_B \frac{\omega_{ce}}{16} \quad (29)$$

In the first case, $\nu_{e,c}$ represents the anticipated scaling with discharge current for classical electron-neutral collisions. We neglect electron–ion collisions, as electron-neutral collisions dominate in the channel [73]. To arrive at this expression and the expression for c_c, we have used the definition of collision frequency as $\nu_{en} = n_n k_{en}$, assumed a constant electron temperature, and expressed the neutral density as $n_n = (\dot{m}_a / v_n m_i A)$. We also have introduced a tunable scaling factor α_c to account for the fact that the actual collision frequency in the thruster channel at typical current densities is orders of magnitude higher than predicted classically [19,74]. This parameter allows us to capture this effect while still retaining the classical scaling of collision frequency with current. The second expression in Eq. (28), $\nu_{e,B}$, represents a Bohm-like scaling for the effective electron collision frequency. This type of model is frequently employed in Hall thruster simulations [19] with a constant scaling parameter α_B that is tuned to better match the simulated electron current with experiment. Unlike the case of classical collision frequency, the Bohm scaling is independent of discharge current.

We can substitute both expressions for collision frequency from Eq. (28) into Eq. (26) to solve for the beam utilization:

$$\eta_{b,c} = \frac{\sqrt{4 a c_c m_i \frac{k_{en}}{\eta_m} I_d + 1} - 1}{2 a c_c m_i \frac{k_{en}}{\eta_m} I_d} \quad \eta_{b,B} = \frac{1}{1 + a c_B \sqrt{m_i}} \quad (30)$$

The first expression of classical scaling for beam utilization suggests that as the discharge current increases, the beam efficiency decreases, whereas the second expression for Bohm-like scaling would indicate that the beam utilization should be independent of current. We plot both of these theoretical results against experimental data in Fig. 13, where we have used best-fit values of $\alpha_c = 20$, $\alpha_B = 0.09$ for xenon and $\alpha_c = 20$, $\alpha_B = 0.14$ for krypton. For both gases, we ultimately see that the experimental values fall between the Bohm and classical scaling. Qualitatively, the classical scaling better captures the decrease in confinement with discharge current for xenon, indicated by a decreasing beam utilization efficiency. However, the classical scaling is too strong, predicting more of a reduction in confinement than exhibited by the plasma. The beam utilization of krypton, on the other hand, has a more Bohm-like trend, as it only slightly decreases and has nearly constant values within uncertainty throughout the range of currents.

The fact that the change in beam utilization has a weaker dependence on current than the classical expectation is a departure from what has previously been proposed for conventional scaling laws in Hall thrusters [14]. This deviation in part explains why the performance did not drop as precipitously as these previous studies have suggested. Indeed, based on our results, we may expect that operating at higher currents beyond what was explored during this effort would only yield moderate decreases in performance. With that said, the transport is also not entirely Bohm-like, particularly for the case of xenon, as the beam utilization does exhibit some dependence on current density. This suggests that the upper bound in performance for these devices may be lower than the limits suggested in recently revised scaling-law studies that assumed a Bohm-like form for the collection frequency [17]. Regardless, from the perspective of informing next steps, these arguments suggest that future efforts should be guided by the assumption that the performance decrease with current density can be bounded by assuming that the electron dynamics fall between these two limits.

3. Trends in Divergence Efficiency

As seen in Fig. 10, the divergence efficiency is generally the second-lowest efficiency mode besides beam utilization, although the values are consistent with other state-of-the-art magnetically shielded Hall thrusters [23,26,27,33]. We note here that magnetically shielded thrusters are known to have slightly higher plume divergence angles, and therefore lower divergence efficiencies, compared to unshielded thrusters. This is because the location of peak magnetic field is shifted downstream in the shielded topology [26], therefore increasing the divergence.

The increase in divergence angle (and corresponding decrease in efficiency) with current for xenon might be attributed to the acceleration region (the narrow area in the thruster channel where most ion acceleration occurs) shifting downstream, thereby increasing plume divergence. This type of correlation between the location of the acceleration zone and divergence angle has previously been noted in Hall thrusters [62,75–77], and a study of the H9 performed with laser-induced fluorescence showed that the acceleration zone was displaced downstream at a discharge current of 30 A, compared to 15 A for both xenon and krypton [70,71]. A similar shift with current density was noted by Reid in an unshielded thruster operating on xenon [61]. Without measurements of the velocity profile within the channel at even higher currents, however, we are unable to conclusively attribute the changes in divergence angle to this effect. Notably, the divergence angle for krypton exhibits a different trend than xenon, staying within a range of 2° throughout the current range. This would suggest in this case that the location of the acceleration zone may not be impacted by the current. With that said, the physical reason for the different trends between the two propellants and its relation to the location of the acceleration zone with current is ultimately unknown.

4. Trends in Overall Anode Efficiency

Equipped with the insights from the preceding section into the processes driving the efficiency modes, we now consider how the convolution of these trends can explain key features in the anode efficiencies of both krypton and xenon. First, our results suggest that the maxima in the efficiencies are the result of a trade between increasing mass utilization and decreasing beam utilization with current. Second, the fact that xenon efficiency exhibits a peak at a
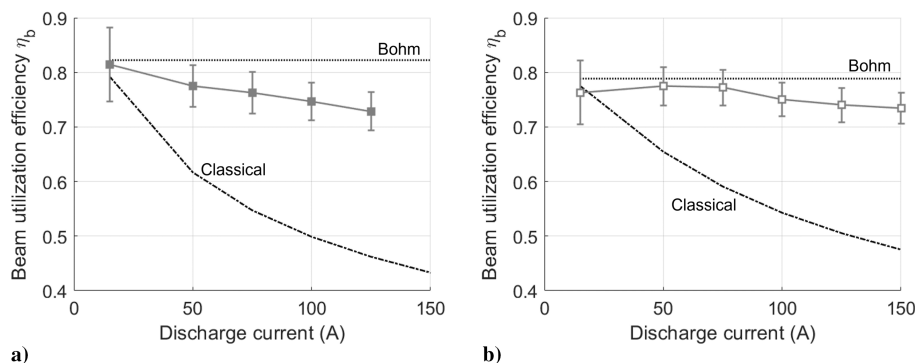

Fig. 13 Experimentally measured beam-current utilization efficiency for a) xenon, and b) krypton operating at 300 V compared to theoretical forms calibrated on data from Table 2.

lower current than krypton can be explained by the fact that higher discharge currents are required for krypton to reach 100% mass utilization due to its higher difficulty of ionization. Because the overall efficiency scales with the product of mass and beam utilization, this has the effect of shifting the peak efficiency to higher currents for krypton. Third, once the mass utilization has achieved 100% efficiency, the beam utilization dominates the overall efficiency curve, leading to an eventual decrease in performance. Krypton's beam utilization declines at a more gradual rate than xenon's, which is responsible for krypton outperforming xenon at sufficiently high currents. Finally, because the mass utilization reaches 100% for both gases and the decrease in beam utilization begins to dominate at higher currents, we anticipate that the performance for both gases will continue to decrease at higher discharge currents. However, it is possible that with lighter, more difficult-to-ionize gases such as Ar or N_2, the peak efficiency would occur at an even higher discharge current than investigated here. These gases may exhibit efficiencies that overtake krypton's and xenon's at sufficiently high current densities, particularly if these lighter propellants have an even more gradual decrease in beam utilization with current than xenon and krypton. This invites new possibilities for the efficient operation of Hall thrusters on these types of alternative propellants [72].

D. Implications for Hall Thrusters as an Option for High-Power EP

We conclude our discussion with a comment on the implications of our results for Hall thrusters as a candidate technology for high-power applications. As discussed in the introduction, the traditional range of Hall thruster thrust density has been a major limitation for scaling to higher power when contrasted with fully electromagnetic concepts like MPD thrusters. Our results have demonstrated that these traditional scaling laws may not be absolute. Indeed, we have shown that the thruster efficiency does not precipitously drop with an approximately 10-times increase in current density compared to the nominal operating condition of the thruster. This corresponds to a six-to-eight-times increase in thrust density for the Hall thruster.

To put this result in the context of alternative technologies for high-power electric propulsion, we show in Fig. 14 the normalized thrust density of the H9 MUSCLE for xenon and krypton compared to thrust densities extracted from a comprehensive database of performance measurements from applied-field MPD thrusters [78]. The cross-sectional area we used to determine thruster density was defined by the solenoid radius for the AF-MPDs and the outer discharge channel radius for the H9 MUSCLE. All results are normalized to the thrust density of the H9 MUSCLE operating on xenon and krypton respectively at 300 V and 15 A. As can be seen from Fig. 14, the performance of the H9 MUSCLE is not only competitive with, but can actually exceed AF-MPD thrust density in this power range. Moreover, the H9 MUSCLE was able to achieve this increase in thrust density while maintaining specific impulses in the range of 2100–2600 s (Fig. 4b) that are desirable for deep space architectures [1]. This is a marked improvement over previous work that focused

on increasing thrust density by increasing Hall thruster voltage [9,10].

We caveat this result with the observation that it is unclear how well this comparison between thrusters holds as the discharge power continues to increase. We may ultimately find, as the trends in our efficiency results suggest (especially the decrease in beam utilization), that performance (and by extension, thrust density) eventually decreases to undesirable limits. However, there may be some margin before this limit is reached, and design decisions such as increased magnetic field strength, decreased discharge voltage, and alternative propellants may help offset these potential losses.

In the context of recent mission studies, the demonstrated performance (Fig. 4) of the H9 MUSCLE from 50 to 100 A for xenon and from 100 to 150 A for krypton satisfy the >50% total efficiency, ~2000-s specific impulse requirements outlined for near-term Mars missions [1]. Although the demonstrated thruster power (45 kW) is under the 2 MW required for these missions, it may be possible to achieve these levels with a single larger unit or by arraying multiple thrusters of the same size. Indeed, a recent study of nuclear architectures suggested that the ideal power level for a 2-MW Hall thruster system may be ~100–200 kW per thruster [3]. For more far-term applications, we demonstrated a thruster-body specific mass of 0.56 kg/kW (compared to ~2.4 kg/kW typically exhibited by Hall thrusters [79]). This metric is approaching the 0.5 kg/kW threshold identified for rapid Mars transit [80], although we note that the mass of the power supply itself remains the dominant challenge in these types of rapid- mission architectures. We caveat this comparison also by commenting that the mass of the cooling system external to the thruster, i.e., the booster pump and heat exchanger, are not included in this specific mass calculation. In practice, the added mass of a thermal management system may nullify the benefits of the reduction in the thruster body's specific mass.

As a final comment, we emphasize that this work was fundamental in nature and performed on a laboratory thruster with a controlled, actively cooled system. Our goal was to test the validity of the traditional arguments about electron confinement at higher current. Practically, transitioning this physics-based experiment to flight has many major technical engineering challenges related to thermal limits as well as magnetic field design. Similarly, the design of hollow cathodes to operate at these enhanced currents may also pose a challenge due to enhanced erosion of the emitter insert. Although longer-life cathodes designed for higher currents certainly exist [81–83], their size may be incompatible with the small form factor of the H9 MUSCLE or similarly scaled-up thrusters.

VI. Conclusions

The goal of this effort was to investigate the fundamental limits of current density scaling in a Hall thruster. This work has been motivated by the increasing interest in developing high-power technologies that may enable nuclear architectures for missions like crewed explorations of Mars. In this context, although Hall thrusters are
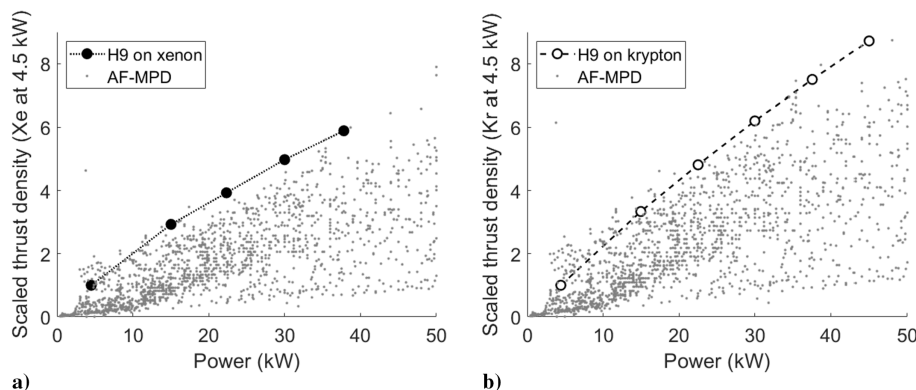

Fig. 14   Comparison of thrust densities scaled to H9 MUSCLE operating on a) xenon, and b) krypton at 4.5 kW compared to results from AF-MPD database [78].

considered a leading candidate technology, one of their primary historic limitations has been their achievable thrust density.

Motivated by recent experimental findings and theoretical studies, we made modifications to a 9-kW-class magnetically shielded laboratory thruster to characterize this device's performance on xenon and krypton from its nominal discharge current of 15 A to a maximum of 150 A. We assessed the global performance measurements of thrust, specific impulse, and efficiency, as well as the efficiency modes of the thruster. Key findings include that (1) the specific impulse increases monotonically for both gases with current; (2) the efficiency decreases at the highest current densities but remains competitive with the performance metrics for conventional Hall thrusters operating at lower powers; and (3) the overall efficiency exhibits an optimum with xenon at 50 A and krypton at 100 A. We have discussed and explained key aspects of these trends with discharge current qualitatively, in the context of simplified scaling laws for thruster operation. For example, we have shown that propellants with lower mass and ionization cross-section, such as krypton in comparison to xenon, are still capable of reaching 100% mass utilization at sufficiently high currents. We also examined the dependence of beam utilization on current, which historically was believed to be the major limitation for operation at high current density. Our findings indicate that the beam utilization does decrease with discharge current but not so precipitously as to preclude competitive efficiencies.

Indeed, our results suggest that the effective electron collision frequency in the channel falls between the limits of classical and Bohm-like scaling. We have also shown that the increasing mass utilization with discharge current combined with the gradual but persistent decrease in beam utilization is what results in a local peak in efficiency for both propellants. The ratio of masses and ionization-rate coefficients for these two propellants is responsible for krypton's peak efficiency occurring at a higher current than xenon.

From a practical perspective, our findings may have implications for future developmental efforts on high-power electric propulsion systems. We have discussed, for example, how operating at a higher current density may enable efficient operation on propellants that have lower ionization cross-sections than xenon. We have also shown that over the power range we investigated, the thrust densities of a Hall thruster can exceed those of a competing technology, the applied-field magnetoplasmadynamic thruster, while still maintaining attractive specific impulse and efficiency. We caveat both of these findings, however, with the remark that it is not certain whether these advantages remain at even higher current densities. It is not clear if and by how much performance will decrease as the thruster operating envelope continues to expand. Indeed, this study was a laboratory demonstration on a laboratory device, and there remain several potentially major challenges with a more practical flightlike implementation. With that said, ultimately, this work represents a critical step in demonstrating how Hall thrusters may be a key enabler for new and exciting capabilities of high-power electric propulsion.

Appendix: Tabulated Thrust and Efficiency Data

Tables A1 and A2 show the values and uncertainties of thrust, specific impulse, anode efficiency, and total efficiency for each condition as inferred from thrust-stand measurements.

Tables A3 and A4 show the values and uncertainties of efficiency modes as inferred from probe measurements.

Table A1   Xenon performance measurements at 300 V

Current, A	Power, kW	Thrust, mN	Isp, s	η_a, %	η_{tot}, %
15	4.5	280 ± 15	1754 ± 98	57.0 ± 7.0	44.6 ± 8.2
50	15	820 ± 19	2174 ± 61	62.1 ± 3.1	54.9 ± 3.8
75	22.5	1100 ± 19	2244 ± 53	57.9 ± 2.3	52.0 ± 2.7
100	30	1394 ± 21	2294 ± 50	55.8 ± 2.0	50.7 ± 2.2
125	37.5	1650 ± 30	2309 ± 56	52.8 ± 2.0	48.2 ± 2.0

Table A2   Krypton performance measurements at 300 V

Current, A	Power, kW	Thrust, mN	Isp, s	η_a, %	η_{tot}, %
15	4.5	211 ± 14	1765 ± 120	44.1 ± 6.0	34.4 ± 6.7
50	15	704 ± 19	2184 ± 69	53.8 ± 2.9	47.5 ± 3.4
75	22.5	1016 ± 19	2331 ± 57	55.1 ± 2.2	49.5 ± 2.6
100	30	1309 ± 22	2465 ± 57	56.3 ± 2.1	51.1 ± 2.3
125	37.5	1582 ± 16	2534 ± 48	55.9 ± 1.7	51.0 ± 1.9
150	45	1839 ± 18	2567 ± 48	55.0 ± 1.6	50.4 ± 1.7

Table A3   Xenon efficiencies from probe measurements at 300 V

Current, A	Power, kW	η_b, %	η_q, %	η_m, %	η_v, %	η_d, %	$\eta_{a,prod}$, %
15	4.5	81.4 ± 6.8	96.9 ± 0.1	88.8 ± 9.6	96.4 ± 2.8	85.4 ± 2.0	57.7 ± 8.1
50	15	77.5 ± 3.9	96.0 ± 0.6	101.2 ± 5.7	95.3 ± 3.5	82.3 ± 1.6	59.0 ± 5.1
75	22.5	76.3 ± 3.8	95.9 ± 1.1	103.4 ± 5.7	96.3 ± 3.5	79.4 ± 1.9	57.8 ± 5.0
100	30	74.7 ± 3.4	96.3 ± 1.7	99.5 ± 5.1	98.1 ± 4.5	78.2 ± 1.6	54.8 ± 4.8
125	37.5	72.8 ± 3.5	96.5 ± 2.1	99.6 ± 5.4	99.5 ± 3.2	77.7 ± 2.2	54.2 ± 4.7

Table A4   Krypton efficiencies from probe measurements at 300 V

Current, A	Power, kW	η_b, %	η_q, %	η_m, %	η_v, %	η_d, %	$\eta_{a,prod}$, %
15	4.5	76.3 ± 5.9	98.8 ± 0.1	78.9 ± 8.2	97.1 ± 3.4	79.0 ± 2.0	45.6 ± 6.2
50	15	77.4 ± 3.5	97.3 ± 0.3	91.7 ± 4.8	94.3 ± 3.7	80.1 ± 1.6	52.2 ± 4.3
75	22.5	77.2 ± 3.3	97.1 ± 0.6	98.0 ± 4.6	93.3 ± 3.5	79.0 ± 1.6	54.2 ± 4.1
100	30	75.0 ± 3.1	96.7 ± 1.0	100.5 ± 4.6	96.3 ± 4.8	79.2 ± 2.0	55.6 ± 4.7
125	37.5	74.0 ± 3.1	96.3 ± 1.7	98.7 ± 4.6	95.8 ± 3.8	79.3 ± 1.9	53.4 ± 4.3
150	45	73.4 ± 2.9	96.2 ± 2.4	98.1 ± 4.4	95.1 ± 3.4	78.1 ± 2.4	51.5 ± 4.1

References

[1] "Space Nuclear Propulsion for Human Mars Exploration," National Academies of Sciences, Engineering, and Medicine TR, Washington, D.C., 2021.
https://doi.org/10.17226/25977

[2] "Next Space Technologies for Exploration Partnerships," NASA Rept. NNH15ZCQ001K, Oct. 2014.

[3] Duchek, M. E., Machemer, W., Harnack, C., Clark, M. A., Pensado, A. R., Palomares, K. B., Polzin, K. A., Martin, A., Curran, F., Myers, R., et al., "Key Performance Parameters for MW-Class NEP Elements and Their Interfaces," *Accelerating Space Commerce, Exploration, and New Discovery*, AIAA Paper 2022-4273, Oct. 2022.
https://doi.org/10.2514/6.2022-4273

[4] Szabo, J., Pote, B., Paintal, S., Robin, M., Hillier, A., Branam, R., and Huffmann, R., "Performance Evaluation of an Iodine-Vapor Hall Thruster," *Journal of Propulsion and Power*, Vol. 28, No. 4, 2012, pp. 848–857.
https://doi.org/10.2514/1.B34291

[5] Pote, B., Hruby, V., and Monheiser, J., "Performance of an 8 kW Hall Thruster," Busek ADA397862, Natick, MA, Jan. 2000.

[6] Xu, K. G., and Walker, M. L., "Effect of External Cathode Azimuthal Position on Hall-Effect Thruster Plume and Diagnostics," *Journal of Propulsion and Power*, Vol. 30, No. 2, 2014, pp. 506–513.
https://doi.org/10.2514/1.B34980

[7] Frieman, J., Gilland, J., Kamhawi, H., Mackey, J., Williams, G., Hofer, R., and Peterson, P., "Wear Trends of the 12.5 kW HERMeS Hall Thruster," *Journal of Applied Physics*, Vol. 130, No. 14, 2021, Paper 143303.
https://doi.org/10.1063/5.0062579

[8] Hall, S. J., Jorns, B. A., Cusson, S. E., Gallimore, A. D., Kamhawi, H., Peterson, P. Y., Haag, T. W., Mackey, J. A., Baird, M. J., and Gilland, J. H., "Performance and High-Speed Characterization of a 100-kW Nested Hall Thruster," *Journal of Propulsion and Power*, Vol. 38, No. 1, 2022, pp. 40–50.
https://doi.org/10.2514/1.B38080

[9] Grishin, S. D., Erofeev, V. S., Zharinov, A. V., Naumkin, V. P., and Safronov, I. V., "Characteristics of a Two-Stage Ion Accelerator with an Anode Layer," *Journal of Applied Mechanics and Technical Physics*, Vol. 19, No. 2, 1978, pp. 166–173.
https://doi.org/10.1007/BF00850027

[10] Sengupta, A., Marrese-Reading, C., Capelli, M., Scharfe, D., Tverdokhlebov, S., Semenkin, S., Tverdokhlebov, O., Boyd, I., Keidar, M., Yalin, A., et al., "An Overview of the VHITAL Program: a Two-Stage Bismuth Fed Very High Specific Impulse Thruster with Anode Layer," *29th International Electric Propulsion Conference*, Paper IEPC-2005-238, Princeton, NJ, Oct. 2005.

[11] Piragino, A., Giannetti, V., Reza, M., Faraji, F., Ferrato, E., Kitaeva, A., Pedrini, D., Andreussi, T., Paganucci, F., and Andrenucci, M., "Development Status of SITAEL's 20 kW Class Hall Thruster," *Propulsion and Energy 2019 Forum*, AIAA Paper 2019-3812, 2019.
https://doi.org/10.2514/6.2019-3812

[12] Giannetti, V., Piragino, A., Paissoni, C., Ferrato, E., Estublier, D., and Andreussi, T., "Experimental Scaling Laws for the Discharge Oscillations and Performance of Hall Thrusters," *Journal of Applied Physics*, Vol. 131, No. 1, 2022, Paper 013304.
https://doi.org/10.1063/5.0070945

[13] Zurbach, S., Cornu, N., and Lasgorceix, P., "Performance Evaluation of a 20 kW Hall Effect Thruster," *32nd International Electric Propulsion Conference*, Paper IEPC-2011-020, Wiesbaden, Germany, 2011.

[14] Dannenmayer, K., and Mazouffre, S., "Elementary Scaling Relations for Hall Effect Thrusters," *Journal of Propulsion and Power*, Vol. 27, No. 1, 2011, pp. 236–245.
https://doi.org/10.2514/1.48382

[15] Morozov, A. I., and Savelyev, V. V., "Fundamentals of Stationary Plasma Thruster Theory," *Reviews of Plasma Physics*, Vol. 21, June 2000, pp. 203–391.
https://doi.org/10.1007/978-1-4615-4309-1_2

[16] Goebel, D. M., and Katz, I., *Fundamentals of Electric Propulsion: Ion and Hall Thrusters*, Jet Propulsion Lab., California Inst. of Technology, Pasadena, CA, 2008.

[17] Simmonds, J., Raitses, Y., and Smolyakov, A., "A Theoretical Thrust Density Limit for Hall Thrusters," *Journal of Electric Propulsion*, Vol. 2, No. 1, 2023, p. 12.
https://doi.org/10.1007/s44205-023-00048-9

[18] Liang, R., "The Combination of Two Concentric Discharge Channels into a Nested Hall-Effect Thruster," Ph.D. Thesis, Univ. of Michigan, Ann Arbor, MI, 2013.

[19] Boeuf, J. P., "Tutorial: Physics and Modeling of Hall Thrusters," *Journal of Applied Physics*, Vol. 121, No. 1, Jan. 2017, Paper 011101.
https://doi.org/10.1063/1.4972269

[20] Su, L. L., and Jorns, B. A., "Performance at High Current Densities of a Magnetically-Shielded Hall Thruster," *Propulsion and Energy 2021 Forum*, AIAA Paper 2021-3405, July 2021.
https://doi.org/10.2514/6.2021-3405

[21] Hofer, R. R., Cusson, S. E., Lobbia, R. B., and Gallimore, A. D., "The H9 Magnetically Shielded Hall Thruster," *35th International Electric Propulsion Conference*, Paper IEPC-2017-232, Atlanta, GA, Oct. 2017.

[22] Cusson, S. E., Hofer, R. R., Lobbia, R., Jorns, B. A., and Gallimore, A. D., "Performance of the H9 Magnetically Shielded Hall Thrusters," *35th International Electric Propulsion Conference*, Paper IEPC-2017-239, Atlanta, GA, Oct. 2017.

[23] Hofer, R. R., Lobbia, R., and Arestie, S., "Performance of a Conducting Wall, Magnetically Shielded Hall Thruster at 3000-s Specific Impulse," *37th International Electric Propulsion Conference*, Paper IEPC-2022-401, Boston, MA, Oct. 2022.

[24] Goebel, D. M., and Watkins, R. M., "Compact Lanthanum Hexaboride Hollow Cathode," *Review of Scientific Instruments*, Vol. 81, No. 8, 2010, Paper 083504.
https://doi.org/10.1063/1.3474921

[25] Mikellides, I. G., Katz, I., Hofer, R. R., and Goebel, D. M., "Magnetic Shielding of a Laboratory Hall Thruster. I. Theory and Validation," *Journal of Applied Physics*, Vol. 115, No. 4, 2014, Paper 043303.
https://doi.org/10.1063/1.4862313

[26] Hofer, R. R., Goebel, D. M., Mikellides, I. G., and Katz, I., "Magnetic Shielding of a Laboratory Hall Thruster. II. Experiments," *Journal of Applied Physics*, Vol. 115, No. 4, 2014, Paper 043304.
https://doi.org/10.1063/1.4862314

[27] Su, L. L., and Jorns, B. A., "Performance Comparison of a 9-kW Magnetically Shielded Hall Thruster Operating on Xenon and Krypton," *Journal of Applied Physics*, Vol. 130, No. 16, 2021, Paper 163306.
https://doi.org/10.1063/5.0066849

[28] Viges, E. A., Jorns, B. A., Gallimore, A. D., and Sheehan, J. P., "University of Michigan's Upgraded Large Vacuum Test Facility," *36th International Electric Propulsion Conference*, Paper IEPC-2019-653, Vienna, Austria, Sept. 2019.

[29] Dankanich, J. W., Walker, M., Swiatek, M. W., and Yim, J. T., "Recommended Practice for Pressure Measurement and Calculation of Effective Pumping Speed in Electric Propulsion Testing," *Journal of Propulsion and Power*, Vol. 33, No. 3, 2017, pp. 668–680.
https://doi.org/10.2514/1.B35478

[30] Yim, J., and Burt, J. M., "Characterization of Vacuum Facility Background Gas Through Simulation and Considerations for Electric Propulsion Ground Testing," *51st Joint Propulsion Conference*, AIAA Paper 2015-3825, 2015.
https://doi.org/10.2514/6.2015-3825

[31] Brown, D. L., and Gallimore, A. D., "Evaluation of Facility Effects on Ion Migration in a Hall Thruster Plume," *Journal of Propulsion and Power*, Vol. 27, No. 3, 2011, pp. 573–585.
https://doi.org/10.2514/1.B34068

[32] Randolph, T., Bekrev, M., Day, M., Fischer, G., Koriakin, A., Kozubsky, K., Krochak, L., Maslennikov, N., Pidgeon, D., Pridannikov, S., et al., "Integrated Test of an SPT-100 Subsystem," *Joint Propulsion Conference and Exhibit*, AIAA Paper 1997-2915, 1997.

[33] Huang, W., Kamhawi, H., and Haag, T., "Facility Effect Characterization Test of NASA's HERMeS Hall Thruster," *52nd Joint Propulsion Conference*, AIAA Paper 2016-4828, July 2016.
https://doi.org/10.2514/6.2016-4828

[34] Xu, K. G., and Walker, M. L., "High-Power, Null-Type, Inverted Pendulum Thrust Stand," *Review of Scientific Instruments*, Vol. 80, No. 5, 2009, Paper 055103.
https://doi.org/10.1063/1.3125626

[35] Polk, J. E., Pancotti, A., Haag, T., King, S., Walker, M., Blakely, J., and Ziemer, J., "Recommended Practice for Thrust Measurement in Electric Propulsion Testing," *Journal of Propulsion and Power*, Vol. 33, No. 3, 2017, pp. 539–555.
https://doi.org/10.2514/1.B35564

[36] Su, L. L., Roberts, P. J., Gill, T., Hurley, W., Marks, T. A., Sercel, C. L., Allen, M., Whittaker, C. B., Byrne, M., Brown, Z., et al., "Operation and Performance of a Magnetically Shielded Hall Thruster at Ultrahigh Current Densities on Xenon and Krypton," *SCITECH 2023 Forum*, AIAA Paper 2023-0842, Jan 2023.
https://doi.org/10.2514/6.2023-0842

[37] Mackey, J., Hall, S. J., Haag, T., Peterson, P. Y., and Kamhawi, H., "Uncertainty in Inverted Pendulum Thrust Measurements," *2018 Joint Propulsion Conference*, AIAA Paper 2018-4516, 2018.
https://doi.org/10.2514/6.2018-4516

[38] Lobbia, R. B., and Beal, B. E., "Recommended Practice for Use of Langmuir Probes in Electric Propulsion Testing," *Journal of Propulsion*

and Power, Vol. 33, No. 3, 2017, pp. 566–581.
https://doi.org/10.2514/1.B35531

[39] Huang, W., Shastry, R., Soulas, G. C., and Kamhawi, H., "Farfield Plume Measurement and Analysis on the NASA-300M and NASA-300MS," *33rd International Electric Propulsion Conference*, Paper IEPC-2013-057, Washington D.C., Oct. 2013.

[40] Efron, B., and Tibshirani, R. J., *An Introduction to the Bootstrap*, CRC Press, Boca Raton, FL, 1994.

[41] Huang, W., and Shastry, R., "Analysis of Wien Filter Spectra from Hall Thruster Plumes," *Review of Scientific Instrumentation*, Vol. 86, No. 7, 2015, Paper 073502.
https://doi.org/10.1063/1.4923282

[42] Shastry, R., Hofer, R. R., Reid, B. M., and Gallimore, A. D., "Method for Analyzing E×B Probe Spectra from Hall Thruster Plumes," *Review of Scientific Instrumentation*, Vol. 80, No. 6, 2009, Paper 063502.
https://doi.org/10.1063/1.3152218

[43] Miller, J., Pullins, S., Levandier, D., Chiu, Y., and Dressler, R., "Xenon Charge Exchange Cross Sections for Electrostatic Thruster Models," *Journal of Applied Physics*, Vol. 91, No. 3, 2002, pp. 984–991.
https://doi.org/10.1063/1.1426246

[44] Hause, M. L., Prince, B. D., and Bemish, R. J., "Krypton Charge Exchange Cross Sections for Hall Effect Thruster Models," *Journal of Applied Physics*, Vol. 113, No. 16, 2013, Paper 163301.
https://doi.org/10.1063/1.4802432

[45] Brown, D. L., Walker, M. L., Szabo, J., Huang, W., and Foster, J. E., "Recommended Practice for Use of Faraday Probes in Electric Propulsion Testing," *Journal of Propulsion and Power*, Vol. 33, No. 3, 2017, pp. 582–613.
https://doi.org/10.2514/1.B35696

[46] Hagstrum, H. D., "Auger Ejection of Electrons from Tungsten by Noble Gas Ions," *Physical Review*, Vol. 96, No. 2, Oct. 1954, p. 325.
https://doi.org/10.1103/PhysRev.96.325

[47] Hagstrum, H. D., "Auger Ejection of Electrons from Molybdenum by Noble Gas Ions," *Physical Review*, Vol. 104, No. 3, July 1956, p. 672.
https://doi.org/10.1103/PhysRev.104.672

[48] Hofer, R. R., and Gallimore, A. D., "Recent Results from Internal and Very-Near-Field Plasma Diagnostics of a High Specific Impulse Hall Thruster," *28th International Electric Propulsion Conference*, Electric Rocket Propulsion Soc., Toulouse, France, 2003, Paper IEPC-2003-037.

[49] Frieman, J. D., Liu, T. M., and Walker, M. L. R., "Background Flow Model of Hall Thruster Neutral Ingestion," *Journal of Propulsion and Power*, Vol. 33, No. 5, Jan. 2017, pp. 1087–1101.
https://doi.org/10.2514/1.b36269

[50] Hall, S. J., "Characterization of a 100-kW Class Nested-Channel Hall Thruster," Ph.D. Thesis, Univ. of Michigan, Ann Arbor, MI, 2018.

[51] Hofer, R. R., and Gallimore, A. D., "High-Specific Impulse Hall Thrusters, Part 2: Efficiency Analysis," *Journal of Propulsion and Power*, Vol. 22, No. 4, 2006, pp. 732–740.
https://doi.org/10.2514/1.15954

[52] Hofer, R., Katz, I., Goebel, D., Jameson, K., Sullivan, R., Johnson, L., and Mikellides, I., "Efficacy of Electron Mobility Models in Hybrid-PIC Hall Thruster Simulations," *44th Joint Propulsion Conference and Exhibit*, AIAA Paper 2008-4924, July 2008.
https://doi.org/10.2514/6.2008-4924

[53] Goebel, D. M., Hofer, R. R., Mikellides, I. G., Katz, I., Polk, J. E., and Dotson, B. N., "Conducting Wall Hall Thrusters," *Institute of Electrical and Electronics Engineers Transactions on Plasma Science*, Vol. 43, No. 1, Jan. 2015, pp. 118–126.
https://doi.org/10.1109/TPS.2014.2321110

[54] Bugrova, A. I., Bishaev, A. M., Desyatskov, A. V., Kozintseva, M. V., Lipatov, A. S., and Dudeck, M., "Experimental Investigations of a Krypton Stationary Plasma Thruster," *International Journal of Aerospace Engineering*, Vol. 2013, March 2013, Paper 686132.
https://doi.org/10.1155/2013/686132

[55] Kurzyna, J., Jakubczak, M., Szelecka, A., and Dannenmayer, K., "Performance Tests of IPPLM's Krypton Hall Thruster," *Laser and Particle Beams*, Vol. 36, No. 1, 2018, pp. 105–114.
https://doi.org/10.1017/S0263034618000046

[56] Linnell, J. A., and Gallimore, A. D., "Efficiency Analysis of a Hall Thruster Operating with Krypton and Xenon," *Journal of Propulsion and Power*, Vol. 22, No. 6, 2006, pp. 1402–1418.
https://doi.org/10.2514/1.19613

[57] Jorns, B. A., Byrne, M., Roberts, P., Su, L., Dale, E., and Hofer, R. R., "Prediction and Mitigation of the Mode Transition in a Magnetically Shielded Hall Thruster at High-Specific Impulse and Low Power," *International Electric Propulsion Conference*, Electric Rocket Propulsion Soc., Boston, MA, 2022.

[58] Kim, V., "Main Physical Features and Processes Determining the Performance of Stationary Plasma Thrusters," *Journal of Propulsion and Power*, Vol. 14, No. 5, 1998, pp. 736–743.
https://doi.org/10.2514/2.5335

[59] Brown, D., Larson, C., Beal, B., and Gallimore, A., "Methodology and Historical Perspective of a Hall Thruster Efficiency Analysis," *Journal of Propulsion and Power*, Vol. 25, No. 6, 2009, pp. 1163–1177.
https://doi.org/10.2514/1.38092

[60] Karadag, B., Cho, S., and Funaki, I., "Thrust Performance, Propellant Ionization, and Thruster Erosion of an External Discharge Plasma Thruster," *Journal of Applied Physics*, Vol. 123, No. 15, 2018, Paper 153302.
https://doi.org/10.1063/1.5023829

[61] Reid, B. M., "The Influence of Neutral Flow Rate in the Operation of Hall Thrusters," Ph.D. Thesis, Univ. of Michigan, Ann Arbor, MI, 2009.

[62] Diamant, K. D., Liang, R., and Corey, R. L., "The Effect of Background Pressure on SPT-100 Hall Thruster Performance," *50th Joint Propulsion Conference*, AIAA Paper 2014-3710, July 2014.
https://doi.org/10.2514/6.2014-3710

[63] Kim, H., Lim, Y., Choe, W., Park, S., and Seon, J., "Effect of Magnetic Field Configuration on the Multiply Charged Ion and Plume Characteristics in Hall Thruster Plasmas," *Applied Physics Letters*, Vol. 106, No. 15, 2015, Paper 154103.
https://doi.org/10.1063/1.4918654

[64] Katz, I., and Mikellides, I. G., "Neutral Gas Free Molecular Flow Algorithm Including Ionization and Walls for Use in Plasma Simulations," *Journal of Computational Physics*, Vol. 230, No. 4, 2011, pp. 1454–1464.
https://doi.org/10.1016/j.jcp.2010.11.013

[65] Pan, R., Ren, J., Mao, R., and Tang, H., "Practical Analysis of Different Neutral Algorithms for Particle Simulation of Hall Thruster," *Plasma Sources Science and Technology*, Vol. 32, No. 3, 2023, Paper 034005.
https://doi.org/10.1088/1361-6595/acc134

[66] Zharinov, A., "Acceleration of Plasma by a Closed Hall Current," *Soviet Physics: Technical Physics*, Vol. 12, 1967, pp. 208–211.

[67] Raitses, Y., Staack, D., Smirnov, A., and Fisch, N., "Space Charge Saturated Sheath Regime and Electron Temperature Saturation in Hall Thrusters," *Physics of Plasmas*, Vol. 12, No. 7, 2005, Paper 073507.
https://doi.org/10.1063/1.1944328

[68] Staack, D., Raitses, Y., and Fisch, N., "Temperature Gradient in Hall Thrusters," *Applied Physics Letters*, Vol. 84, No. 16, 2004, pp. 3028–3030.
https://doi.org/10.1063/1.1710732

[69] Reid, B., and Gallimore, A., "Plasma Potential Measurements in the Discharge Channel of a 6-kW Hall Thruster," *44th Joint Propulsion Conference and Exhibit*, AIAA Paper 2008-5185, July 2008.
https://doi.org/10.2514/6.2008-5185

[70] Su, L., "Performance of a Magnetically Shielded Hall Thruster Operating on Krypton at High Powers," Ph.D. Thesis, Univ. of Michigan, Ann Arbor, MI, 2023.

[71] Su, L., Marks, T., and Jorns, B., "Investigation into the Efficiency Gap Between Krypton and Xenon Operation on a Magnetically Shielded Hall Thruster," *37th International Electric Propulsion Conference*, Paper IEPC-2022-366, Boston, MA, June 2022.

[72] Marchioni, F., and Cappelli, M. A., "Extended Channel Hall Thruster for Air-Breathing Electric Propulsion," *Journal of Applied Physics*, Vol. 130, No. 5, 2021, Paper 053306.
https://doi.org/10.1063/5.0048283

[73] Mikellides, I. G., and Ortega, A. L., "Challenges in the Development and Verification of First-Principles Models in Hall-Effect Thruster Simulations that are Based on Anomalous Resistivity and Generalized Ohm's law," *Plasma Sources Science and Technology*, Vol. 28, No. 1, 2019, Paper 014003.

[74] Marks, T. A., and Jorns, B. A., "Challenges with the Self-Consistent Implementation of Closure Models for Anomalous Electron Transport in Fluid Simulations of Hall Thrusters," *Plasma Sources Science and Technology*, Vol. 32, No. 4, 2023, Paper 045016.
https://doi.org/10.1088/1361-6595/accd18

[75] Cusson, S. E., Dale, E. T., Jorns, B. A., and Gallimore, A. D., "Acceleration Region Dynamics in a Magnetically Shielded Hall Thruster," *Physics of Plasmas*, Vol. 26, No. 2, 2019, Paper 023506.
https://doi.org/10.1063/1.5079414

[76] Nakles, M. R., and Hargus, W. A., Jr., "Background Pressure Effects on Ion Velocity Distribution Within a Medium-Power Hall Thruster," *Journal of Propulsion and Power*, Vol. 27, No. 4, 2011, pp. 737–743.
https://doi.org/10.2514/1.48027

[77] MacDonald-Tenenbaum, N., Pratt, Q., Nakles, M., Pilgram, N., Holmes, M., and Hargus, W., Jr., "Background Pressure Effects on Ion Velocity Distributions in an SPT-100 Hall Thruster," *Journal of Propulsion and*

Power, Vol. 35, No. 2, 2019, pp. 403–412.
https://doi.org/10.2514/1.B37133

[78] Electric Propulsion and Plasma Dynamics Laboratory, *AF-MPD Thruster Database*, Princeton Univ., Princeton, NJ, 2022, https://alfven.princeton.edu/tools/afmpdt-database/.

[79] Hofer, R. R., and Randolph, T. M., "Mass and Cost Model for Selecting Thruster Size in Electric Propulsion Systems," *Journal of Propulsion and Power*, Vol. 29, No. 1, 2013, pp. 166–177.
https://doi.org/10.2514/1.B34525

[80] Dankanich, J. W., Vondra, B., and Ilin, A. V., "Fast Transits to Mars Using Electric Propulsion," *46th Joint Propulsion Conference and Exhibit*, AIAA Paper 2010-6771, July 2010.
https://doi.org/10.2514/6.2010-6771

[81] Becatti, G., Goebel, D. M., Yoke, C. V., Ortega, A. L., and Mikellides, I. G., "High Current Hollow Cathode for the X3 100-kW Class Nested Hall Thruster," *36th International Electric Propulsion Conference*, Paper IEPC-2019-371, 2019.

[82] Becatti, G., Goebel, D. M., and Zuin, M., "Observation of Rotating Magnetohydrodynamic Modes in the Plume of a High-Current Hollow Cathode," *Journal of Applied Physics*, Vol. 129, No. 3, 2021, Paper 033304.
https://doi.org/10.1063/5.0028566

[83] Becatti, G., and Goebel, D. M., "500-A LaB6 Hollow Cathode for High Power Electric Thrusters," *Vacuum*, Vol. 198, April 2022, Paper 110895.
https://doi.org/10.1016/j.vacuum.2022.110895

J. Rovey
Associate Editor